Solar Physics
DOI: 10.1007/●●●●●-●●●-●●●-●●●●-●

# Development of a Fast CME and Properties of a Related Interplanetary Transient

**V.V. Grechnev[1] · A.A. Kochanov[1] · A.M. Uralov[1] · V.A. Slemzin[2] · D.G. Rodkin[2] · F.F. Goryaev[2] · V.I. Kiselev[1] · I.I. Myshyakov[1]**

Received ; accepted



**Abstract** We study the development of a coronal mass ejection (CME) caused by a prominence eruption on 24 February 2011 and properties of a related interplanetary CME (ICME). The prominence destabilized, accelerated, and produced an M3.5 flare, a fast CME, and a shock wave. The eruption at the east limb was observed in quadrature by the *Atmospheric Imaging Assembly* (AIA) on board the *Solar Dynamics Observatory* (SDO) and by the *Sun Earth Connection Coronal and Heliospheric Investigation* (SECCHI) instrument suite on board the *Solar-Terrestrial Relations Observatory* (STEREO). The ICME produced by the SOL2011-02-24 event was measured *in situ* on STEREO-B two days later. The diagnostics made from multi-wavelength SDO/AIA images reveals a pre-eruptive heating of the prominence to about 7 MK and its subsequent heating during the eruption by flare-accelerated particles to about 10 MK. The hot plasma was detected in the related ICME as an enhancement in the ionic charge state of Fe, whose evolution was reproduced in the modeling. The analysis of the solar source region allows predicting the variations of magnetic components in the ICME, while the flux-rope rotation by about 40° was indicated by observations. The magnetic-cloud propagation appears to be ballistic.

✉ V.V. Grechnev
grechnev@iszf.irk.ru

A.A. Kochanov
kochanov@iszf.irk.ru

A.M. Uralov
uralov@iszf.irk.ru

V.A. Slemzin
slemzinva@lebedev.ru

[1] Institute of Solar-Terrestrial Physics SB RAS, Lermontov St. 126A, Irkutsk 664033, Russia

[2] Lebedev Physical Institute (LPI), Leninsky Prospect 53, Moscow, 119991, Russia

**Keywords:** Coronal Mass Ejections; Heating, in Flares; Magnetic fields, Interplanetary; Prominences, Active; Solar Wind, Disturbances; X-Ray Bursts

## 1. Introduction

Coronal mass ejections (CMEs) are the most magnificent manifestation of sporadic solar activity. CMEs originate in the corona, expand, and travel far in the heliosphere, where they are termed interplanetary CMEs (ICMEs: *e.g.* Richardson and Cane, 2010; Démoulin, 2010; Manchester *et al.*, 2017). CMEs are often accompanied by flares and shock waves that can produce energetic particles. CMEs/ICMEs carry magnetized plasma; if an ICME impacts the Earth's magnetosphere, then geomagnetic disturbances may occur. The strongest geomagnetic storms are caused by ICMEs with a southward $B_z$ component. All of these products of solar activity pose hazards to modern technology systems.

One possible driver of a CME and flare is a flux rope. It is identified with a magnetic cloud (MC) in the ICME structure. The ability of flux ropes to drive CMEs was shown theoretically (Anzer, 1978; Chen, 1996; Gibson and Low, 1998; Amari *et al.*, 2000; Démoulin and Aulanier, 2010; Lin, Gallagher, and Raftery, 2010; Chen, 2017). The CME launch can be associated with the eruption of a prominence (*e.g.* Švestka, 2001; Uralov *et al.*, 2002; Filippov, 2013; Grechnev *et al.*, 2015) or a sigmoid visible in extreme ultraviolet (EUV) or soft X-rays (SXR) (*e.g.* Canfield, Hudson, and McKenzie, 1999; James *et al.*, 2017). Tether-cutting reconnection (Moore *et al.*, 2001) and flux cancellation are possible mechanisms for the formation from these structures of flux ropes and their pre-eruptive heating which, along with plasma heating during the eruption, can supply a significant fraction to the CME energy budget (*e.g.* Lee *et al.*, 2009; Landi *et al.*, 2010; Murphy, Raymond, and Korreck, 2011).

The association of CMEs with prominence eruptions indicates a possible inheritance of plasma confined in their bodies. ICMEs as counterparts of near-Sun CMEs can be identified *in situ* by specific plasma and magnetic characteristics (*e.g.* Zurbuchen and Richardson, 2006). Important signatures of ICME plasma are anomalies in charge states of heavy ions. The ionic compositional marks provide a useful tool to identify ICMEs (Richardson and Cane, 2004, 2010). Enhanced Fe charge states often observed in the solar wind provide an identifier of ICMEs and evidence of magnetic relationship to flaring regions (*e.g.* Lepri *et al.*, 2001; Lepri and Zurbuchen, 2004; Rodkin *et al.*, 2018).

To predict parameters of CMEs/ICMEs, the processes of their development and the patterns that govern their propagation in the interplanetary space should be known. Statistical relations have been found between the CME speed and magnetic field strength in an associated ICME (Yurchyshyn, Hu, and Abramenko, 2005). The quantitative correspondence between the flare-reconnected magnetic flux and magnetic field in the ICME was established by Qiu *et al.* (2007). Statistical correspondence was found between the magnetic flux involved in an eruption and some parameters of CMEs and geospace disturbances (Qiu and Yurchyshyn, 2005; Chertok *et al.*, 2013; Chertok, Grechnev, and Abunin, 2017; Gopalswamy *et al.*, 2017; Pal *et al.*, 2018).

Nevertheless, unanswered questions remain about particular processes responsible for the CME development and subsequent ICME propagation that can be complicated by the influence of different ICMEs (Shen *et al.*, 2012; Rollett *et al.*, 2014). The sign of the $B_z$ component in a ICME escapes certain predicting. Fast MCs are expected to be decelerated in the solar wind by the aerodynamic drag force (*e.g.* Cargill, 2004; Aschwanden and Gopalswamy, 2019), but it does not seem to be always significant (*e.g.* Manchester *et al.*, 2008; Wood, Howard, and Linton, 2016). The existing numerical and analytical models (*e.g.* Odstrcil, 2003; Vršnak *et al.*, 2013, 2014; Jian *et al.*, 2015; Mays *et al.*, 2015) have large uncertainties in the ICME arrival time and velocity and meet difficulties in predicting the magnetic-field parameters. One of possible ways to improve their forecast is to invoke observations of the early CME formation stage that are available due to routine solar imaging in EUV and different (see, *e.g.*, Foullon *et al.*, 2007; Liu *et al.*, 2010).

In view of these challenges, we analyze the solar eruptive event which occurred on 24 February 2011 and the ICME that it produced. From the analysis of the solar eruption and observations of the CME we endeavor to find main properties of the ICME and compare the actual measurements *in situ* with the expectations. The choice of the event is determined by the following circumstances:

i) The event was observed in quadrature by the *Atmospheric Imaging Assembly* (AIA) on board the *Solar Dynamics Observatory* (SDO: Lemen *et al.*, 2012) and by the *Sun Earth Connection Coronal and Heliospheric Investigation* instrument suite (SECCHI: Howard *et al.*, 2008) on the Behind spacecraft of the twin *Solar-Terrestrial Relations Observatory* (STEREO: Kaiser *et al.*, 2008).

ii) The position of the source region N15 E84 favors the measurements above the limb from AIA images without overlap with on-disk structures. The only disadvantage of the near-the-limb position is the absence of simultaneous high-quality magnetograms from the *Helioseismic and Magnetic Imager* (HMI: Scherrer *et al.*, 2012) on board SDO.

iii) The eruption produced a CME directed to STEREO-B that was located 94.6° eastward from Earth. The corresponding ICME reached STEREO-B on 26 February and was measured *in situ* by the *Plasma and Suprathermal Ion Composition* (PLASTIC) investigation (Galvin *et al.*, 2008) and the magnetometer (MAG: Acuña *et al.*, 2008) of the *In situ Measurements of PArticles and CME Transients* (IMPACT: Luhmann *et al.*, 2008).

iv) Several aspects of this event have been known due to preceding studies.

The differential emission measure (DEM) of flaring loops during the M3.5 flare was evaluated by Battaglia and Kontar (2012). Martínez Oliveros *et al.* (2012) found that this flare was a white-light flare and evaluated the heights of the hard X-ray (HXR) and white-light sources above the photosphere. Kumar *et al.* (2012) analyzed the eruption and concluded that the prominence accelerated due to the torus instability. Möstl, Temmer, and Veronig (2013) studied manifestations of

the Kelvin–Helmholtz instability at the boundaries of the erupting prominence. Shen *et al.* (2014) analyzed the dynamics of the flaring and peripheral loops. Grechnev *et al.* (2015) concluded that the prominence eruption initiated the flare and drove the CME and a shock wave. Some properties of the SOL2011-02-24 event, including impulsive $\gamma$-ray emission up to 1 MeV, are listed in the catalog of $\gamma$-ray flares presented by Share *et al.* (2018).

To shed light on the CME development and to relate the ICME with its solar progenitor, we analyze their kinematics, magnetic structures and high-temperature marks. The solar event is outlined in Section 2. Taking account of the results obtained previously, we examine in Sections 3 and 4 the chain of phenomena that determined the properties of the ICME. Following the CME genesis, we consider its launch, magnetic structure, heating, and the ionic charge-state of iron. Then we compare the expectations for the ICME with actual *in situ* measurements, in particular the magnetic flux-rope structure and orientation. The ionic charge-state of iron in the MC plasma indicates its origin in the erupting prominence. Calculations confirm that the high ionic charge-state of Fe in the MC agrees with heating of the erupting structures during the impulsive acceleration stage. Section A in Appendix considers general dependencies of the charge-state freeze-in process on plasma parameters and CME velocity. The event and measurements are illustrated by the movies in the Electronic Supplementary Material. Section 5 summarizes our approaches that have led to the following results:

The flux rope probably developed from magnetic structures of an eruptive prominence and inherited its plasma, which underwent two stages of heating. The flux rope became the CME core and, eventually, the magnetic cloud in the ICME.

A local pre-eruptive heating was possibly caused by electric currents that manifested in an increasing SXR flux. The heating resulted in a considerable increase in the plasma pressure that could be significant in driving the sharp eruption.

The eruption started first, and then the flare emission appeared. During the flare impulsive phase, the brightness of the erupting prominence correlated with the HXR flux. The erupting structures were heated up to about 10 MK possibly by accelerated electrons injected from the reconnection site. Part of these electrons remained trapped in the erupting structures and probably produced a Type IV burst.

The model calculations show that a large fraction of Fe ions with a charge $Z \geq 16$ in the ICME was produced due to both strong heating in the eruption and high CME velocity that was rapidly acquired. The modeling also shows that the bi-modality of the Fe-ion charge-state distribution may be an intrinsic property of ICMEs.

The MC structure inherited properties of its solar progenitor and could be predicted. The flux rope rotated by $\approx 40^\circ$ not far from the Sun that is detectable from coronagraph observations. The transit of the CME core (MC) from the Sun to STEREO-B seems to be ballistic.

## 2. Overview of the Solar Eruptive Event

The solar event on 24 February 2011 comprised a prominence eruption and an M3.5 flare that occurred around 07:30 (all times hereafter refer to UTC). The event was visible from two vantage points. From the Earth's direction, the event was observed on the east limb (N15 E84) in particular by SDO/AIA, the *Reuven Ramaty High-Energy Solar Spectroscopic Imager* (RHESSI: Lin *et al.*, 2002), and the *Large Angle and Spectroscopic Coronagraph* (LASCO: Brueckner *et al.*, 1995) on board the *Solar and Heliospheric Observatory* (SOHO: Domingo, Fleck, and Poland, 1995). From STEREO-B located 94.6° eastward from the Sun-Earth line at a heliocentric distance of 1.02 AU, the eruptive flare was visible not far from solar disk center. AIA movies of the event can be found at hesperia.gsfc.nasa.gov/sdo/aia/movies/2011/02/24/20110224_0721-0820/. STEREO movies are available at cdaw.gsfc.nasa.gov/stereo/daily_movies/2011/02/24/. LASCO movies of the CME are available at cdaw.gsfc.nasa.gov/CME_list/daily_movies/2011/02/24/.

Figure 1 presents a view of the event from the Earth's direction (right column) and a view from the left for STEREO-B/SECCHI (left column). A combination of full-disk AIA image ratios observed in the 211 Å and 304 Å channels in Figure 1b shows the erupting prominence and a northerly set of steady loops. The inset in Figure 1b shows an enlarged image of the erupting prominence in 304 Å. The equator indicates the tilt of the solar axis to the Sun–Earth line. The solar disk center had a latitude of $B_0 = -7.13°$, whose absolute value was close to the total tilt of the solar axis to the ecliptic (7.25°). To make the ecliptic horizontal, the images in Figures 1a and 1c were rotated counter-clockwise by 7°.

The 195 Å image in Figure 1a produced by the *Extreme Ultraviolet Imager* (EUVI: Howard *et al.*, 2008) on board STEREO-B shows that the eruption site in active region (AR) 11163 was located at the southwestern part of a train constituted by AR 11163 and AR 11164. A large coronal hole adjoined the train from the west. The eruption produced an EUV wave visible as a faint arc-like feature expanding to the east and south (above the "EUV wave" label). The EUV wave propagated over a large area, including the Earth-facing solar surface.

In association with the eruption, a strong flare developed. Its emission caused saturation of EUVI visible in the inset in Figure 1a as a set of bright streaks. The saturation hampered the EUVI observations of the flare arcade for almost one hour. A strong burst was observed in HXR and $\gamma$-rays up to 1 MeV.

The eruption gave rise to a fast main CME shown in Figures 1c and 1d. According to the online CME catalog (cdaw.gsfc.nasa.gov/CME_list/: Yashiro *et al.*, 2004), it had an average speed of $\approx 1190\,\mathrm{km\,s^{-1}}$ and strongly decelerated ($-22\,\mathrm{m\,s^{-2}}$). The direction of the erupting prominence was initially non-radial (the shorter arrow in Figure 1d) and then gradually changed to the final orientation of the fast CME (the longer arrow) corresponding to a position angle (PA) of 96° listed in the CME catalog. The fast CME collided with a slow CME (at a PA $\approx 120°$) and deflected it (see the movies in the CME catalog).

The brighter southern part of the main CME is distinct at a longer distance as a partial halo in a STEREO-B/COR2 image in Figure 1c, while its northern part is not detectable. Following the impulsive eruption around 07:30, the plasma outflow was observed by AIA in 304 Å for more than two hours. The erupted

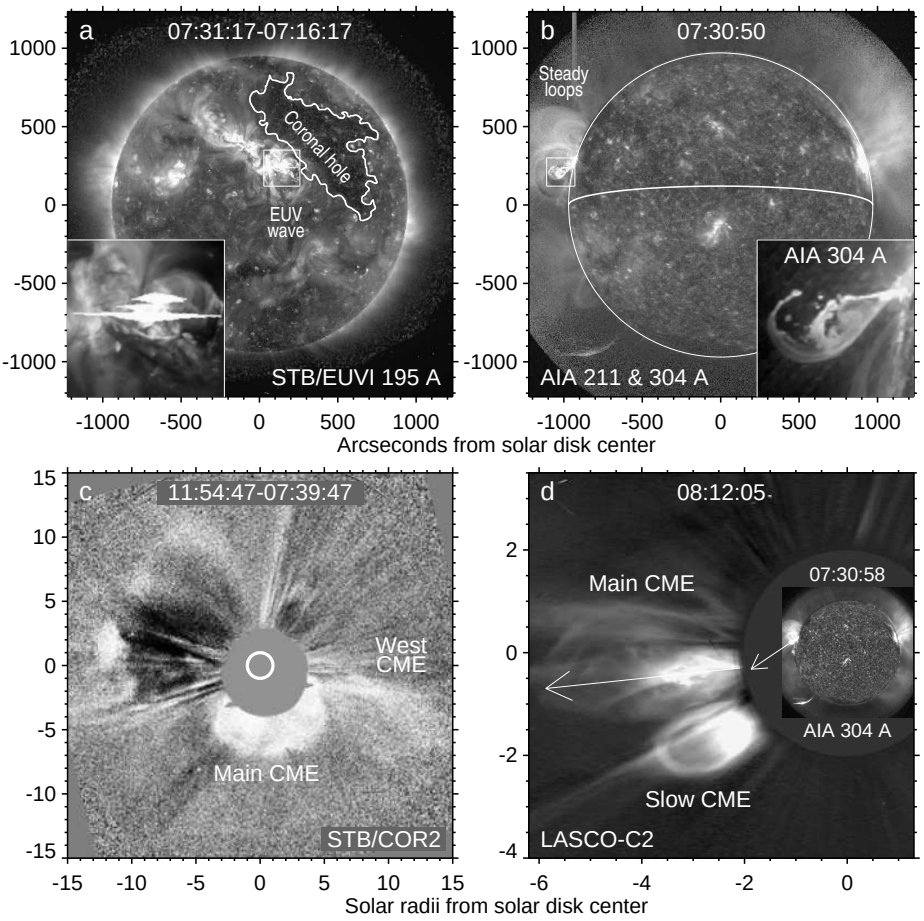


**Figure 1.** Overview of the event. (**a**) Eruption in a STEREO-B/EUVI 195 Å image. The *contour* outlines a coronal hole. Enlarged image of the flare site is shown in the *inset*, whose position is presented by the *frame*. (**b**) Eruption in a combined SDO/AIA 211 Å and 304 Å image. The *equator* indicates the orientation of the solar axis. Enlarged image of the erupting prominence is shown in the *inset*, whose position is indicated by the *frame*. (**c**) The main CME directed to STEREO-B and a minor west CME in a STEREO-B/COR2 image. (**d**) Main CME observed by LASCO-C2 during the collision with a slow CME. The *inset* shows the erupting prominence in an earlier SDO/AIA 304 Å image at its actual position. The *short arrow* represents the initial direction of the erupting prominence. The *long arrow* indicates the direction of the main CME. The *circles* in panels **b** and **c** denote solar limb. The horizontal direction is parallel to the ecliptic. Solar north is up in the right panels.

material partly returned to the solar surface. Then, around 07:52, AIA images show another accelerating twisted bright structure. New flare ribbons appeared at that time in the 1700 Å AIA images and weaker HXR and microwave bursts occurred. The secondary eruption is visible in the movies presented by Shen *et al.* (2014). A west CME moving away in Figure 1c was probably a result of this eruption and most likely did not reach STEREO-B.

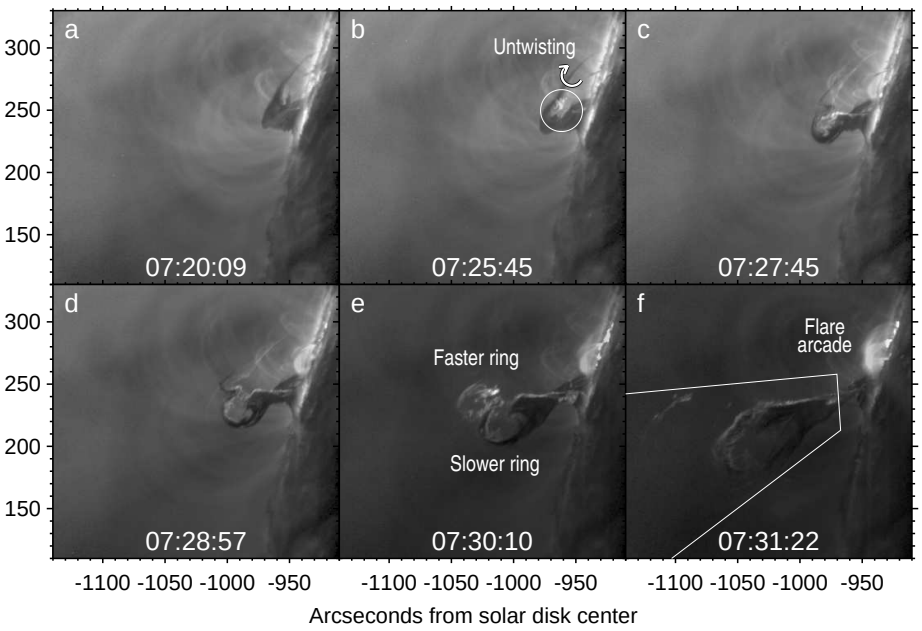


**Figure 2.** Episodes of the prominence eruption in comparison with the development of the flare arcade in 193 Å AIA images, each of which is presented in an individual nonlinear brightness scale. (**a**) Prominence before the acceleration stage. (**b**) Onset of prominence heating. The *circle* marks the region where the average brightness shown in Figure 8 was measured. The *round arrow* indicates the prominence untwisting. (**c**) Eruption starts. Flare arcade appears. (**d**) Two ring-like segments appear. (**e**) The faster ring brightens up and accelerates. (**f**) Both rings acquire high velocities. The faster ring fades. The *white tetragon* denotes the region where the average brightness shown in Figure 9 was measured.

## 3. Prominence Eruption and CME

Figure 2 presents episodes of the prominence eruption in the SDO/AIA 193 Å images. The prominence activated more than half an hour that was manifested in a steady increase in the soft X-ray (SXR) flux recorded by GOES in 1 – 8 Å (Grechnev *et al.*, 2015). Figure 2a shows the prominence shortly before the eruption. The circled prominence part brightens in Figure 2b. The northern prominence leg untwisted during 07:24 – 07:26 in the direction indicated by the circular arrow, as the AIA_171_193_untwisting.mpg Electronic Supplementary Material shows.

The prominence liftoff begins in Figure 2c. The northern prominence leg bents, transforming into a ring-like structure. Flare loops appear. The northern ring strongly accelerates in Figure 2d, brightens up in Figure 2e and becomes the fastest structure. The body of the slower ring is still dark; only its edges become brighter. The faster ring rapidly expands and disappears in Figure 2f. The slower ring also acquires considerable velocity. The flare arcade becomes clearly visible.

The prominence body in Figures 2a – 2d is considerably darker than the environment and screens coronal structures behind it. This situation is observed in all AIA channels that are dominated by iron emission lines. Such a large absorption

depth is only possible due to the photo-ionization of hydrogen and helium in the prominence material, if its temperature does not exceed $2 \times 10^4$ K (Anzer and Heinzel, 2005). The faster prominence ring becomes bright and transparent in all AIA channels (Figure 2e) that indicates its heating up to at least 1 MK.

The temperature of a heated prominence can be estimated using the DEM inversion from multi-channel AIA images. To estimate the DEM of a fast feature correctly avoiding the appearance of spurious hot regions at its edges, expansion should be compensated for according to its kinematics (Grechnev *et al.*, 2016). We had to refine the kinematical measurements made for this event by Grechnev *et al.* (2015) from AIA 211 Å images in a short time interval that did not allow us to "stop" the rings with an accuracy required for a correct DEM inversion.

### 3.1. Kinematics

We measured the kinematics for different erupting components from AIA images in 304, 171, 211, 131, and 195 Å, coordinating the results with each other. The Electronic Supplementary Material AIA_304_orig_resized_faster_ring.mpg and AIA_304_orig_resized_slower_ring.mpg movies are composed from original 304 Å images (left) and resized images (right) to make static one of the rings, as indicated by the names of the movies. Figure 3 shows 304 Å images, in which the slower ring is stopped according to the kinematical plots presented in Figure 4.

Comparison with Figure 2 and movies indicates the presence of both cool and hot plasma in the erupting prominence and its envelope. The 304 Å images reveal a "wrapper" that enveloped both rings and consisted of loops rooted near the ends of the prominence. The wrapper is distinct after 07:27 in 304 Å only that indicates its temperature of $< 1$ MK at that time. In all of the figures and movies, the solid lines correspond to the faster ring, the dashed lines correspond to the slower ring, and the dotted lines correspond to the wrapper.

We fitted the accelerations for the leading edges of erupting features with two to three Gaussian pulses and adjusted their parameters to keep the features in the resized movies static. The AIA_131_193_304_resized.mpg Electronic Supplementary Material presents the acceleration plots and the AIA images in 131, 193, and 304 Å resized according to the measured distance–time plots. The expansion of the rings is compensated for satisfactorily from 07:28 to 07:31 that allows measuring the DEM within this interval.

The measurements are limited by the AIA field of view and by the visibility of the erupting components. The faster ring was not defined initially, more or less formed to 07:28, and disappeared after 07:32. Two acceleration episodes of the faster ring with a half-height duration of about one minute occurred earlier than the corresponding HXR peaks 1 and 2 by about 120 and 40 seconds, respectively (Figures 4c and 4d). The highest acceleration peak reached $\approx 11\,\mathrm{km\,s^{-2}}$. Each acceleration episode affected both rings and the wrapper. When the faster ring faded, the slower ring and wrapper underwent a third acceleration episode. Because the erupting features left the AIA field of view soon, the uncertainties in the thin-gray extrapolated kinematical plots in Figures 4a – 4c are large.

The initial orientation of the erupting prominence of $-47°$ relative to the East direction (straight-dotted line in Figures 3a and 3f) gradually changed to $-24°$

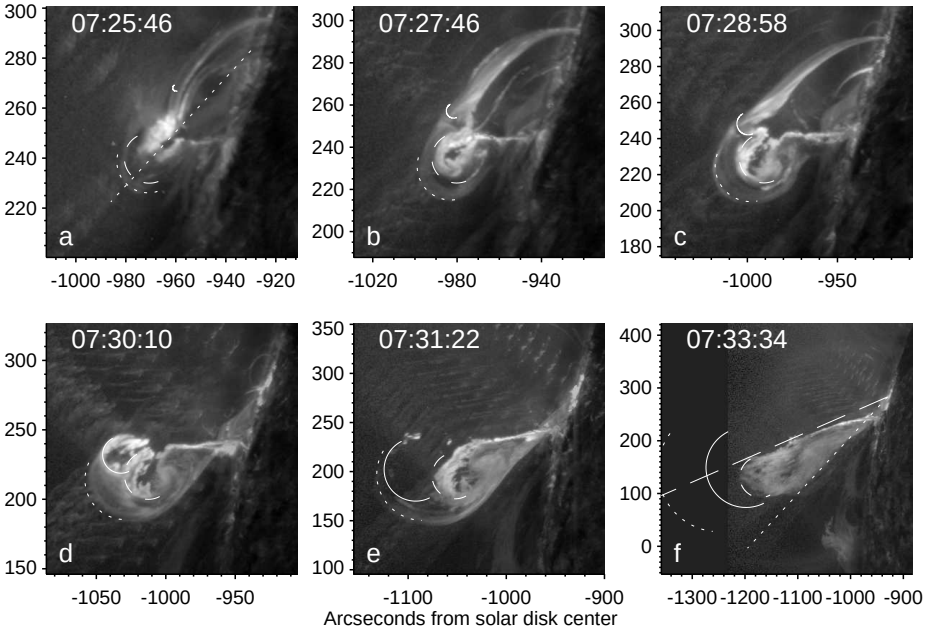


**Figure 3.** Prominence eruption in AIA 304 Å images resized according to the kinematics shown in Figure 4a. The field of view is resized to keep the size of the slower ring unchanged. The *arcs* outline the three erupting components: faster ring (*solid*), slower ring (*dashed*), and wrapper (*dotted*). The line styles correspond to Figure 4. The *dotted straight line* in panels **a** and **f** marks the initial orientation of the prominence of $-47°$ from the East direction. The *dashed straight line* in panel **f** marks the final direction of the eruption in AIA images ($-24°$). The observation times in panels **a**–**e** correspond to the AIA 193 Å images in Figures 2b – 2f.

within the AIA field of view. Finally, the CME orientation became about $-6°$ relative to the east direction that corresponds to a PA of 96°.

Thus, the eruption process developed from below. While the curled rings belonged to a forming active flux-rope structure, the simple loops of the wrapper appear to have been pushed by the trailing rings, as Figure 4a and the movies suggest. Initially, these loops probably enveloped the pre-eruptive prominence.

### 3.2. EUV Wave

To analyze the DEM of erupting structures, the coronal background should be known. With an acceleration of up to $\approx 11\,\mathrm{km\,s^{-2}}$, the erupting prominence produced a disturbance, which rapidly became a shock wave. According to Grechnev *et al.* (2015), it was impulsively excited at 07:29:00 ±20 seconds. The shock wave was manifested in a Type II burst, a halo ahead of the CME body, and an "EUV wave". The EUV wave is visible in Figure 5 as a bright compressed layer of swept-up plasma far ahead of the erupting prominence and wrapper. The EUV wave is distinct in 211 Å and 193 Å, being not clearly visible in other AIA channels that indicates its temperature of $\approx 2$ MK.

The expansion of a large loop system that surrounded the erupting prominence lagged behind its motion. The response of the outer loop denoted in

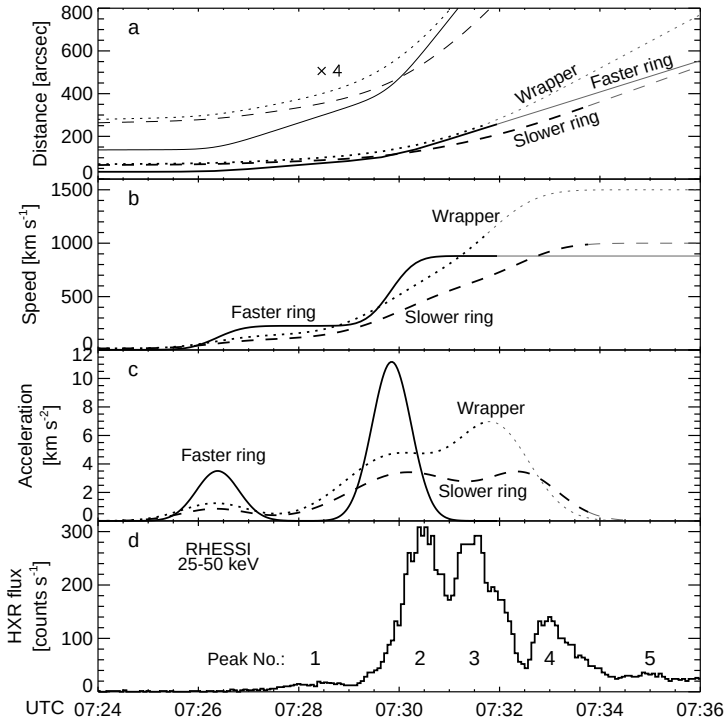


**Figure 4.** Kinematics measured for three erupting components: faster ring (*solid*), slower ring (*dashed*), and wrapper (*dotted*). The *thin-gray* parts of the curves indicate when the features became invisible. (**a**) Distance–time plot. The *thin-black* curves show the initial parts of the plots magnified by a factor of four. (**b**) Velocity–time plot. (**c**) Acceleration–time plot. (**d**) HXR burst recorded by RHESSI in the 25 – 50 keV range. *Labels 1 – 5* denote separate HXR peaks.

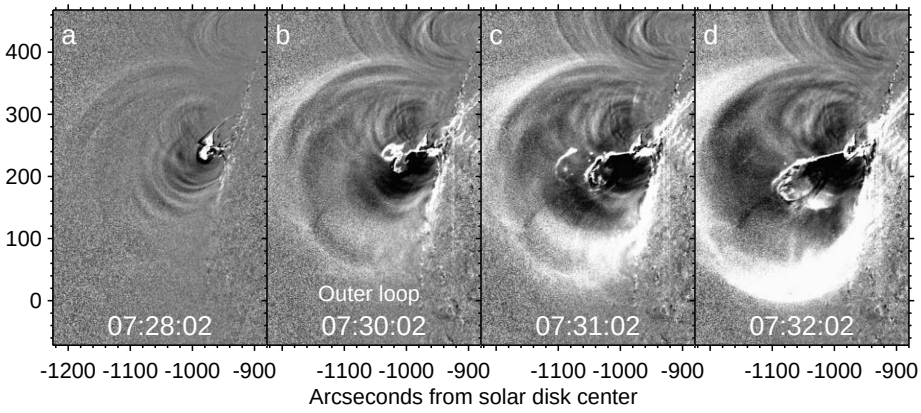


**Figure 5.** EUV wave produced by the prominence eruption visible in the AIA 211 Å image ratios. The image in each panel is a result of dividing the original AIA image by a fixed AIA image observed at 07:27:02. Progressive darkening represents the developing dimming.

Figure 5b relative to the wave onset time at the erupting prominence corresponds to a wave propagation speed of $\approx 1500\,\mathrm{km\,s^{-1}}$. Subsequent expansion of the shock wave was observed as a halo ahead of the CME body.

### 3.3. Differential Emission Measure

We used for the DEM inversion the method and software developed by Plowman, Kankelborg, and Martens (2013). The input images in the six AIA channels that are dominated by iron emission lines were preprocessed. First, the stray-light correction was made by means of the point-spread function deconvolution using the aia_deconvolve_richardsonlucy routine. Second, the standard aia_prep routine was applied. The DEM was analyzed for the initial interval (07:22–07:29) without a compensation for the motion of the prominence, whose displacement between successive images was insignificant. The compensation for its rapid motion after 07:29 used the distance–time plots shown in Figure 4a. The DEM cubes were analyzed from the column emission measure *vs.* temperature profiles averaged over hot regions. The temperatures $< 1\,\mathrm{MK}$ were not considered.

The DEM profiles for the initial interval were calculated for a bright region of untwisting and for a thin bright layer that surrounded the prominence, as shown in Figure 6a. The profiles show the main peak at $\approx 2\,\mathrm{MK}$ and a second peak or shoulder at $\approx 7\,\mathrm{MK}$ as high as $0.4-0.7$ of the main peak. The main peak represents the quiet corona integrated along the line of sight in front of the prominence with a contribution from the compressed layer behind the EUV wave front. This layer visible in Figure 5 probably surrounded the erupting prominence on all sides. To separate the hot peak, we subtracted a profile averaged over an offset circular region of $24''$ in diameter. The result is not perfect because of nonuniform plasma distribution over the compressed layer, developing dimming, and screening by the prominence of the coronal emission behind it.

The DEM image at 07:23 in Figure 6a was summed over the temperature layers from 5 MK to 14 MK. The regions analyzed are denoted by the color contours. The dotted circle denotes the region where the background was measured. Figure 6b presents the DEM profiles averaged over the contoured regions. We keep the DEM scaling *vs.* $\log_{10}(T)$ provided by the Plowman, Kankelborg, and Martens (2013) software, because dividing the profiles by $T\ln(10)$ to convert to the conventional units of $\mathrm{cm^{-5}\,K^{-1}}$ makes the hot peak less distinct.

The thick-solid background-subtracted DEM profiles in Figure 6b reveal in the untwisting region (red) a hot component with a temperature of $\approx 7\,\mathrm{MK}$ that persisted during the initial interval. The thin prominence envelope (blue) also had a temperature of $\approx 7\,\mathrm{MK}$. The hot components probably reveal the regions of energy release. A result of heating expected as a broad lower-temperature enhancement in the profiles is difficult to detect reliably because of a large background contribution in this temperature range. A peak at $\approx 3\,\mathrm{MK}$ persisting from 07:22 to 07:26 within this range is open to question.

The average column emission measure of the hot component in the untwisting region monotonically rose by 80% from 07:22 to 07:27 that is consistent with an increase in the SXR flux in Figure 8. Figure 6a reveals additional heated sites, *e.g.* beneath the untwisting region, that we did not consider. Battaglia and Kontar

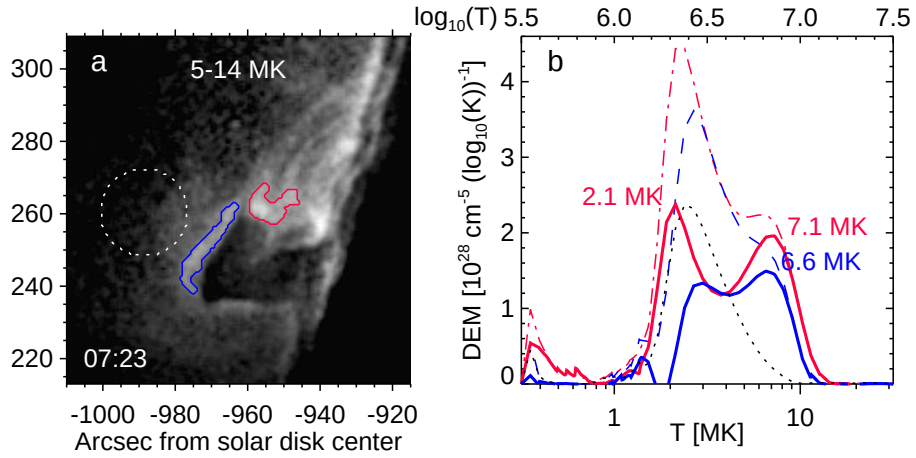


**Figure 6.** DEM analysis of the initial heating at 07:23. (**a**) The image of the DEM summed over a temperature range of 5 – 14 MK. The *red contour* outlines the bright region of untwisting, the *blue contour* selects a portion of the heated prominence envelope, and the *dotted circle* denotes the background region. (**b**) Averaged column emission measure *vs.* temperature profiles computed for the *contoured* regions shown in panel **a** by the same *colors*. The *dotted line* shows the background. The *thin-broken lines* represent the profiles without background subtraction. The *thick-solid lines* represent the background-subtracted DEM profiles.

(2012) found for a coronal source located there a temperature of $\approx 8$ MK and emission measure increasing after 07:20. The complexity of the shapes of the heated regions that are rather poorly defined and large uncertainties in their depths hamper reliable estimations of their total emission measure and densities.

The temperature increase in the parts of the prominence body from the initial value of $T \leq 2 \times 10^4$ K up to $T \approx 7$ MK results in an increase in the plasma pressure, $2nkT$, by a factor of $\gtrsim 350$, if the number density of electrons and ions $[n]$ is constant. If the prominence material was initially not fully ionized, then the pressure increase must be still stronger.

The DEM analysis for the impulsive acceleration stage was made using the compensation for the motion of the faster ring. At 07:32, when the faster ring faded, both rings had comparable velocities that allows analyzing the DEM of the slower ring using the same compensation. The result is shown in Figure 7.

The peak temperature of the hot component in Figure 7b is 8.1 MK and its average temperature weighted with DEM is 8.5 MK. The area within the contours in Figure 7a is $A \approx 4 \times 10^{18}$ cm$^2$. The total emission measure in this volume is EM $\approx 6 \times 10^{44}$ cm$^{-3}$. The average width of the contoured part is $\approx 5''$. With a high thermal pressure inside the ring, its depth $[h]$ is expected to be comparable with the width, *i.e.* $h \approx 4 \times 10^8$ cm. Then, the electron number density of the hot component in the slower ring at 07:32 was $n_e \approx \sqrt{\mathrm{EM}/(A\,h)} \approx 6 \times 10^8$ cm$^{-3}$ presumably within a factor of four.

The temperature of the hot component in the faster ring was estimated in a similar way at 07:29, 07:30, and 07:31; the density was only estimated for the two last times, when the faster ring was formed. Table 1 lists the parameters estimated for the rings along with an expansion factor $[k_{\mathrm{exp}}]$ calculated for the

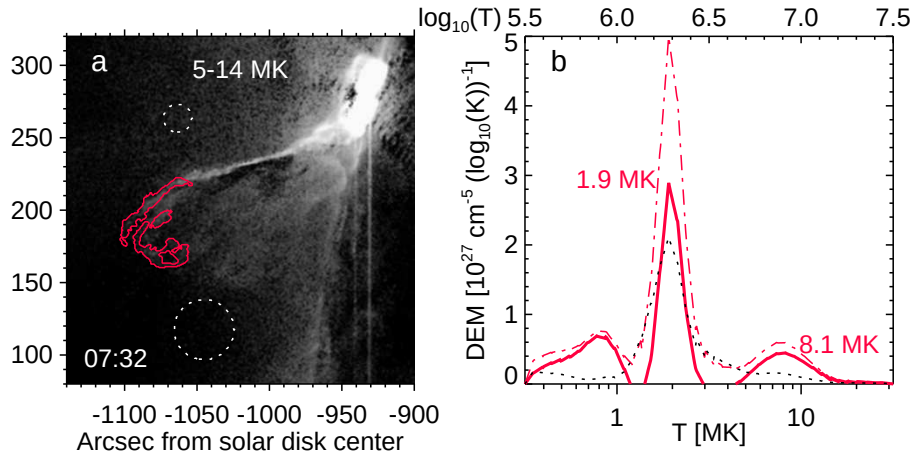


**Figure 7.** DEM computed for the slower ring observed at 07:32 in the format similar to Figure 6. Two circular regions shown in panel **a** were used here to estimate the background.

**Table 1.** Parameters of the hot component estimated for the erupting structures.

| Time [UTC] | $d$ [Mm] | $T$ [MK] | $n_e$ [cm$^{-3}$] | $k_{exp}$ |
|---|---|---|---|---|
| Faster ring | | | | |
| 07:29 | 56 | 9 | – | 2.39 |
| 07:30 | 76 | 10 | $2 \times 10^9$ | 3.25 |
| 07:31 | 116 | 12 | $8 \times 10^8$ | 4.92 |
| Slower ring | | | | |
| 07:32 | 132 | 8 | $6 \times 10^8$ | 3.23 |

center of each ring as a ratio of its distance [$d$] from the expansion center at a corresponding time to the distance that it had at 07:23.

The density in an erupting structure is expected to decrease as $k_{exp}^{-3}$. The ratio of the densities in the faster ring estimated at 07:30 and 07:31 is 2.5, while the expected ratio is 3.5; the difference is within the errors. We similarly estimate the density in the pre-eruptive prominence. The initial density back-extrapolated from the density estimated for the faster ring at 07:30 is $2 \times 10^9 \times 3.25^3 \approx 7 \times 10^{10}$ cm$^{-3}$ and about $1 \times 10^{11}$ cm$^{-3}$ from the estimate obtained at 07:31. Referring to the slower ring at 07:32, we estimate the initial density of $2 \times 10^{10}$ cm$^{-3}$. Probably, the slower ring was not yet heated entirely at 07:32, unlike the faster ring that was totally bright after 07:29. If so, then the estimate of $2 \times 10^{10}$ cm$^{-3}$ provides a lower limit for the initial prominence density.

### 3.4. Heating of the Eruptive Prominence

Two heating mechanisms seem to be at work: heating at the initiation stage by electric currents and heating of the erupting prominence by flare-accelerated

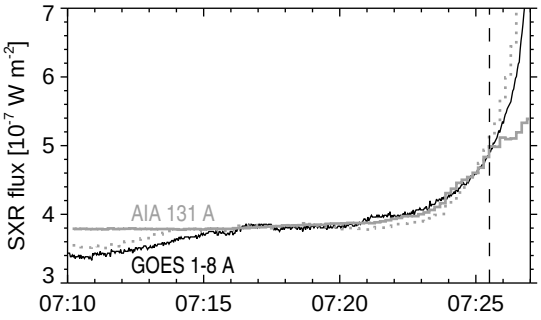


**Figure 8.** The brightness of the pre-eruptive prominence in 131 Å in comparison with the SXR flux in 1 – 8 Å (*black*). The average prominence brightness was measured within the *circular region* shown in Figure 2b (*gray-solid*) and a larger area including the flare site (*gray-dotted*). The temporal profiles in 131 Å are scaled to match the SXR flux. The correlation between the prominence brightness and SXR flux diminishes after 07:25:30 (*vertical dashed line*).

electrons. Figure 8 compares the brightness of a pre-eruptive prominence in 131 Å and the SXR flux in 1 – 8 Å (black line). The solid-gray line represents the average prominence brightness within the circled region in Figure 2b without the flare arcade. The dotted-gray line shows the average brightness over a broader area of $307'' \times 307''$ with the same center, including the flare arcade. This temporal profile corresponds to the variations in the SXR flux. The circled prominence part is also similar to the SXR flux from 07:16:30 to 07:25:30 (*cf.* Grechnev *et al.*, 2016), and then the correspondence disappears.

As the AIA_131_193_HXR.mpg Electronic Supplementary Material indicates, the erupting components brightened roughly during HXR peaks. To verify this indication, we computed the average brightness in 131 Å and 193 Å images over a tetragonal region shown in Figure 2f that encloses the erupting filament without the flare arcade. The 131 Å images are affected by scattered light from the flare that produces an increasing trend. The temporal profile in 193 Å has a declining trend caused by a developing dimming. Figure 9 compares de-trended EUV temporal profiles with the HXR burst. Four out of five HXR peaks have counterparts in the EUV temporal profiles. The only exception is HXR peak 4 that occurred when the faster ring faded in all AIA channels; thus, it vanished unlikely because of temperature variations. Possibly, HXR peak 4 corresponded to a brightening of the faster ring, which faded because of a rapid expansion.

As long as the prominence was static, manifestations of its heating in Figure 8 corresponded to the SXR flux variations. The character of heating changed when the prominence liftoff started; the heating episodes in Figure 9 became synchronous with the HXR peaks that suggests heating of the erupting prominence by flare-accelerated particles at this stage.

As the DEM analysis shows, the local pre-eruptive heating up to about 7 MK occurred in the untwisting prominence leg and the thin prominence envelope (the skin-heating of eruptive prominences was reported previously, *e.g.*, by Grechnev *et al.*, 2006). The initial prominence heating was accompanied by its slow motion (see the Electronic Supplementary Material and Grechnev *et al.*, 2015), being probably responsible for a gradual rise of the SXR flux, as Zhang *et al.* (2001)

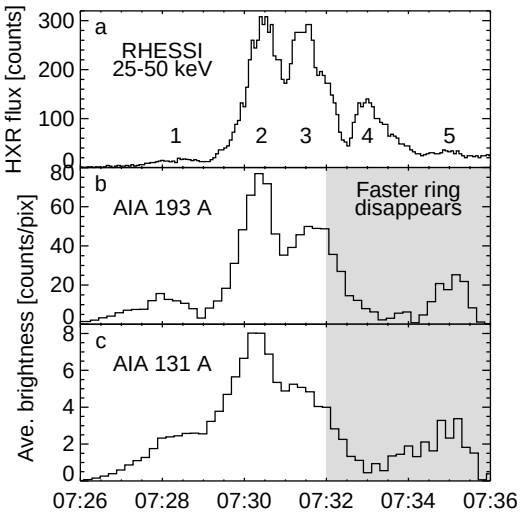


**Figure 9.** Brightness of the erupting prominence in comparison with the HXR burst recorded by RHESSI at 25 – 50 keV (**a**). *Labels 1 – 5* denote separate HXR peaks. (**b**, **c**) De-trended average brightness of the erupting prominence in 193 Å (**b**) and in 131 Å (**c**) over the *tetragonal region* denoted in Figure 2f. The *shading* indicates when the faster ring disappeared.

conjectured. The heating might be caused by electric currents due to initial reconnection between the prominence threads (see Grechnev *et al.*, 2015 for discussion) and be significant in driving the eruption.

In the impulsive acceleration stage, considerable parts of the erupting components underwent a rapid heating up to 8 – 12 MK. At this stage, the expansion of the prominence becomes important; if no source of heating had been present, then the erupting prominence cooled down. The heating by electric current becomes inefficient at this stage. The ohmic loss per one thermal plasma particle is $j^2/(\sigma N)$ with $j \propto \nabla \times B$ being the current density, $\sigma \propto T^{3/2}$ being the Coulomb conductivity, $N$ the number density of thermal particles with a temperature of $T$, and $B$ the magnetic field strength. In the erupting prominence, $B \propto k_{\rm exp}^{-2}$ and $N \propto k_{\rm exp}^{-3}$, where $k_{\rm exp}$ is the expansion factor. The energy acquired by one thermal particle per second is $\propto k_{\rm exp}^{-3} T^{-3/2}$. The role of ohmic losses rapidly decreases in the expansion and heating of the erupting prominence. The contribution from ohmic losses was largest before the eruption, while the bulk of the prominence material was at a low temperature. The heating of the expanding prominence by ohmic losses is less significant.

On the other hand, numerous electrons accelerated by flare processes appear at this stage. In the course of flare reconnection, accelerated electrons are injected both down, into the flare loops, and up, into the forming flux rope (see, *e.g.*, Masson, Antiochos, and DeVore (2013) for the scenario). The heating by electrons accelerated by flare processes is indicated by the correspondence between the average brightness of the eruption in EUV and the HXR flux in Figure 9. The braking of flare-accelerated electrons in the cool, dense plasma of the erupting prominence is somewhat similar to their interaction with the chromosphere.

Heating of CMEs, particularly cores, was reported previously. Landi *et al.* (2010) and Murphy, Raymond, and Korreck (2011) found heating to be significant in the energy budget of a CME and discussed possible heating mechanisms, but their observations were inconclusive. Analyzing the HXR source in a moving CME core, Glesener *et al.* (2013) concluded that the collisional heating by flare-accelerated electrons was the most probable heating mechanism. It was sufficient to provide the observed thermal energy to the core, whose temperature was $\approx 11$ MK, comparable with our estimates. Glesener *et al.* (2013) demonstrated the CME-core heating by flare-accelerated electrons; our event complements the overall scenario by the CME-core development from the erupting filament.

While most accelerated electrons injected into the erupting prominence (CME core) thermalize, some higher-energy electrons escape collisions and remain confined, being governed by the processes occurring in a magnetic trap (*e.g.* Metcalf and Alexander, 1999), which rapidly expands in this situation. This population shows up in a Type IV burst that was observed by the *Radio and Plasma Wave Investigation* (S/WAVES: Bougeret *et al.*, 2008) on board STEREO-B (cdaw.gsfc.nasa.gov/stereo/daily_movies/2011/02/24/) from 08:10 to 08:50 at frequencies $> 10$ MHz. This plasma frequency puts the upper limit of $n_e \lesssim 1.4 \times 10^6\,\mathrm{cm}^{-3}$ to the electron number density in the core (see Section 4.2).

### 3.5. Magnetic-Field Direction

In a typical situation of an inverse configuration of the erupted prominence represented by the standard flare model, the azimuthal magnetic field in the leading part of a flux rope is expected to correspond to the magnetic-field direction in a post-eruption arcade. Figure 10a presents a pre-eruptive prominence observed as a dark filament by STEREO-B/EUVI in 304 Å. The broken magnetic neutral line extrapolated at 26 Mm traces the filament. Figure 10b shows the flare arcade one hour after the flare, when saturation ceased. The longer eastern loops of a different orientation appeared after the secondary eruption around 07:52 and were not related to the main eruption or the M3.5 flare.

To find the magnetic-field direction in the arcade loops, a magnetogram is required. Since AR 11163 that hosted the eruptive flare was located close to the limb, where magnetograms are strongly distorted, we had to use a magnetogram observed later. However, a rapid decay of AR 11163 changed the magnetic-field distribution relative to the event occurrence time. We used an SDO/HMI vector magnetogram with resolved $\pi$-ambiguity observed two days after the flare, when AR 11163 displaced far enough from the limb. The coronal magnetic field was obtained using potential extrapolation. The neutral line at a height of 26 Mm above the photosphere acceptably matches the filament in Figures 10a and 10b. Hence, the potential-field structure of AR 11163 did not change drastically during the two days that allows us to rely to some extent on the later-days magnetograms.

Figure 10c presents the distributions of the normal and tangential components of the photosphere field obtained from an HMI magnetogram and reprojected to the viewing direction from STEREO-B. The tangential component has a nearly western direction along the neutral line in the central part of the arcade in

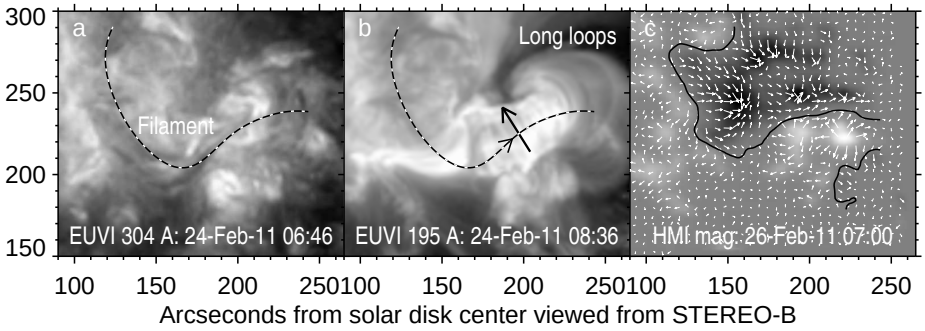


**Figure 10.** Magnetic-field direction. (**a**) Pre-eruptive filament in EUVI 304 Å image. The *broken line* in panels **a** and **b** is the neutral line extrapolated at 26 Mm. (**b**) Flare arcade in a late post-eruption image. The *straight arrow* indicates the magnetic polarity of the arcade loops. The arrow at the neutral line indicates the direction of the axial field. The eastern loops with a different orientation were insignificant in the main flare. The *long loops* were not involved in the eruption. (**c**) Vector magnetogram observed by SDO/HMI two days later and transformed to the viewing direction from STEREO-B at the event occurrence time: the *gray-scale* image shows the radial component (*bright* positive, *dark* negative), the *arrows* present the tangential component). The *black contour* is the neutral line extrapolated at 2 Mm. Solar north is up.

Figure 10b. This direction of the tangential component along with the fact that magnetic field is positive to the south from the neutral line and negative to the north indicates the left handedness of the magnetic flux rope in the coronal volume above the neutral line. A different quantity indicating the handedness is the current helicity $H_{\rm c}$ that is defined as

$$H_{\rm c} = \int \boldsymbol{J} \cdot \boldsymbol{B}\, dV,$$

where $\boldsymbol{J}$ is the electric-current density and $\boldsymbol{B}$ is magnetic field. Since the potential extrapolation is current-free, we use a proxy quantity for $H_{\rm c}$ defined as

$$H_{\rm c}^{n} = \int J_n B_n \, dS,$$

where $J_n$ and $B_n$ are the normal components of the current density and magnetic field, respectively; the integration is carried out over the photospheric surface that contains the active region. $J_n$ can be calculated using the tangential component. The calculations made from the HMI vector magnetograms obtained on 25 and 26 February show that the negative component of $H_{\rm c}^{n}$ exceeded the positive component by a factor of about 1.5 that also indicates the left-handed twist.

These indications determine the magnetic-field direction in the arcade loops shown by the arrows in Figure 10b. The tilt of the neutral line to the west–east direction at the arrow is $\approx 41^\circ$. With an angle between the horizontal axis in Figure 10 and ecliptic plane of $\approx 7^\circ$, the expected orientation of the flux-rope axis is $\psi \approx 42^\circ$ clockwise from the ecliptic north pole.

There are different indications at the flux-rope handedness. The counter-clockwise untwisting motion of the erupting prominence visible in the AIA_171_193_untwisting.mpg Electronic Supplementary Material and indicated in Figure 2b, if looking at the northern prominence end along its leg, corresponds to an opposite prominence twist. This can be seen from an example of a twisted rubber rope, whose ends are fastened and the top pulled up. The clockwise prominence twist indicates the direction of its axial magnetic component toward the northern end, *i.e.* from south–east to north–west in Figure 10. This direction corresponds to the left handedness of the prominence and the flux rope.

Figures 10b and 10c provide another indication. The magnetic field in the eastern arcade formed after the secondary eruption was directed from South–East to North–West. The eastern end of this arcade shared the magnetic polarity with the eastern end of the filament that erupted in the main event that confirms the direction of the axial magnetic component shown by the arrow in Figure 10b.

The heading part of a magnetic cloud (MC) can be approximated in a simplest case with a force-free magnetic cylinder (Marubashi *et al.*, 2015; see Figure 17 for a scheme). Relating this geometry to Figure 10, we suggest some qualitative expectations for the MC produced in this event: *i*) The axial magnetic component is directed toward the northern ecliptic hemisphere. If the MC had been Earth-directed, then its geomagnetic effect would not be strong, while the magnetic field in the sheath is difficult to predict; *ii*) The MC is left-handed.

Figure 1 and the results of this sections allow outlining expected variations of magnetic components in the MC. The magnetic cylinder probably hits STEREO-B by its northern part. In this situation, the radial magnetic component is expected to be directed always sunward. The perpendicular magnetic component in the ecliptic plane is initially directed eastward and becomes westward-directed in the trailing half of the MC. The magnetic component perpendicular to the ecliptic plane is expected to be directed northward in the leading part of the MC and to change the direction in its trailing part; the magnetic-field strength there must be reduced according to the expansion factor squared. The actual *in situ* observations are compared with the expectations in Section 4.1.

### 3.6. CMEs

To determine the roles of three CMEs observed by coronagraphs, we consider the signatures of the CMEs in 304 Å images obtained from different vantage points. Figure 11 presents nearly simultaneous observations of the event in 304 Å by STEREO-B/EUVI (left column) and by SDO/AIA (right column). The direction of a CME is indicated by erupted material in its wake. The erupted material screening the solar disk in EUVI images is dark and bright in AIA images.

Figures 11a and 11d correspond to the appearance of the main CME in the LASCO-C2 field of view. A dark spot in Figure 11a indicates a southward CME direction (long arrow). Figure 11b reveals the signatures of a secondary eruption that occurred around 07:52 and bifurcated in Figure 11c. One of its parts detectable above the limb moved southwest probably following the west CME. Another part of the bifurcated eruption moved south. A corresponding ejection could have joined the trailing part of the main CME.

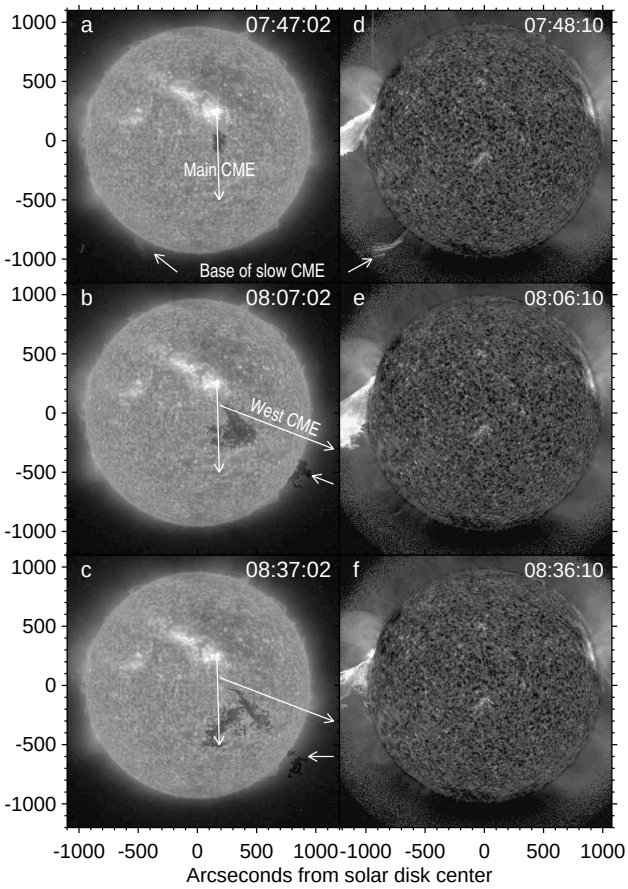


**Figure 11.** Manifestations of the eruptions observed in 304 Å from the vantage points of STEREO-B (*left column*) and SDO (*right column*). (**a**–**c**) Dark absorbing material in contrasted EUVI images. The *long southward arrow* indicates the direction of the main CME. The *long southwestward arrow* indicates the direction of the west CME in Figure 1c. The *short arrows* in the top panels indicate an erupting prominence at the base of the slow CME. The *short arrows* in panels **b** and **c** indicate an off-limb dark material in the wake of the west CME. (**d**–**f**) Bright erupted material visible in contrasted AIA images above the east limb.

The dispersal of erupted material over a large surface far from the eruption site was first identified by Slemzin *et al.* (2004). Such phenomena are observed less often than material draining along the legs of an erupted prominence. The dispersal is probably caused by reconnection between the magnetic structure of an eruption and static coronal environment (Grechnev *et al.*, 2005, 2013, 2014; Uralov *et al.*, 2014) that could account for the observations shown in Figure 11.

Figures 11a and 11d show an erupting prominence at the base of the slow CME that was located at the far side of the Sun. The main, fast CME appeared in Figure 12a at 07:48. It stressed and deflected the slow CME (Figure 12d). After the collision, the slow CME returned to its initial orientation. A peripheral collision with a slow CME also unlikely affected the main CME significantly.

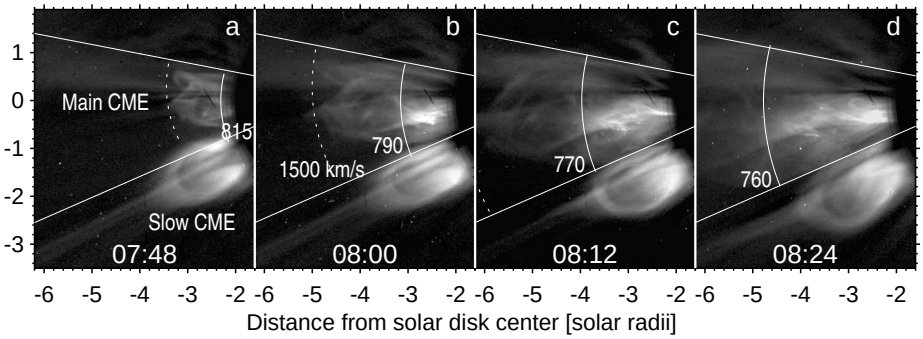


**Figure 12.** Main CME and its collision with a slow CME observed by LASCO-C2. The *straight lines* represent the angular width of the main CME of 35°. The *dashed arc* outlines the frontal structure moving with a speed of about $1500\,\mathrm{km\,s^{-1}}$. The *solid arc* outlines the decelerating core, whose instantaneous speed is indicated at the arcs.

The main CME had an angular width of $\theta \approx 35°$ within the straight lines in Figure 12 and a central angle of $\phi \approx -6°$ south from the east direction. The outermost CME component was its shell, the frontal structure (FS); the shock front was ahead it (Grechnev *et al.*, 2015). The FS probably consisted of the coronal loops visible in Figure 5 high above the erupting prominence and the loops of the wrapper, having the same velocity of $\approx 1500\,\mathrm{km\,s^{-1}}$ (Figure 4). The FS was followed by a brighter intertwisted core that was presumably formed from the erupted prominence and had a velocity comparable with the final velocities of the rings of $900-1000\,\mathrm{km\,s^{-1}}$ in Figure 4. The gap between the core and FS (often observed as a cavity) had a low brightness that indicates reduced-density plasma, probably with magnetic field frozen-in.

So far kinematics has mostly been measured for leading edges of CMEs. To analyze the motion of the core inside a CME, an approximate description of its kinematics is helpful. CMEs are affected by several propelling and retarding forces (see, *e.g.*, Low, 1982; Chen, 1989, 1996; Chen and Krall, 2003). We extremely simplify the situation and consider only gravity at this point. It follows from the total kinetic plus potential energy conservation:

$$v_1^2 = v_0^2 - 2G\mathrm{M}_\odot(1/r_0 - 1/r_1) \tag{1}$$

with $v_0$ ($v_1$) being a velocity of the body at a distance $r_0$ ($r_1$) from the Sun's center, $G$ the universal gravity constant, and $\mathrm{M}_\odot$ the mass of the Sun. Using Equation 1, we calculated the ballistic kinematics for the CME core with a given initial velocity $v_0$ at $2\,\mathrm{R}_\odot$ until the arrival at the STEREO-B orbit (1.02 AU). Figure 13 shows the velocity–distance plots for $v_0 = 830\,\mathrm{km\,s^{-1}} \pm 5\,\%$. The time when the core reached a heliocentric distance of $2\,\mathrm{R}_\odot$ was taken 07:44:12. The expected time of the CME core arrival at STEREO-B is indicated in the figure. A change of $\pm 5\,\%$ in the value of $v_0 = 830\,\mathrm{km\,s^{-1}}$ changes the arrival time by about $\mp 4$ hours. The gravitational deceleration mainly ceases within $30\,\mathrm{R}_\odot$.

The solid arcs in Figure 12 corresponding to the thick-solid line in Figure 13 acceptably outline the core. The core velocity of $830\,\mathrm{km\,s^{-1}}$ at a distance of $2\,\mathrm{R}_\odot$

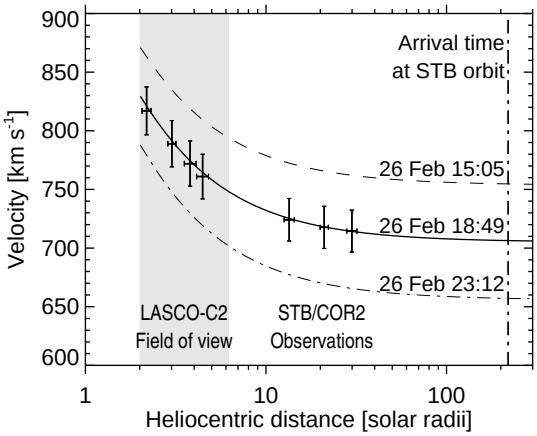


**Figure 13.** Velocity–distance plots for a ballistic motion of the CME core from $2R_\odot$ to the orbit of STEREO-B (*vertical dash-dotted line*): probable motion with $v_0 = 830\,\mathrm{km\,s^{-1}}$ and for $v_0 \pm 5\,\%$ (*dashed* and *dash-dotted*). The *crossed bars* directly represent the measurements with uncertainties from LASCO-C2 images in Figure 12 within the shaded interval and from STEREO-B/COR2 images in Figure 14 with a projection correction.

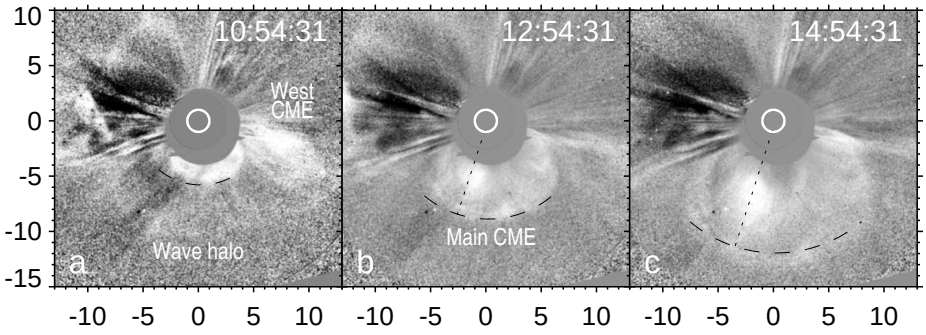


**Figure 14.** The main CME and west CME in STEREO-B/COR2 images. Each panel presents a ratio between the current image and the COR2 image observed at 07:39:31. The *circles* denote solar limb. The *dashed arcs* outlining the main CME were calculated from the kinematics shown in Figure 13 with a projection correction. The *dotted radial lines* in panels **b** and **c** denote a presumable flux-rope orientation of $\psi \approx 17°$ clockwise from the Ecliptic South Pole.

seems to be consistent with the velocities measured for the erupting-prominence rings of $900 - 1000\,\mathrm{km\,s^{-1}}$ at $0.4\,R_\odot$ in Figure 4.

Figure 14 presents three STEREO-B/COR2 images. The main CME appears as a partial halo south from the ecliptic plane and directed to STEREO-B in the horizontal plane. Figure 14a also shows the west CME and a halo-like wave trace (see Grechnev *et al.*, 2015 for details). The identification of the main-CME structural components from the COR2 images is not reliable; nevertheless, an extended bright blob in Figures 14b and 14c might be the core associated with the flux rope. The orientation of the blob's radial axis is $\psi \approx 17°$.

Thus, the main CME observed by LASCO had an angular width of $\theta \approx 35°$ and a central angle relative to the east of $\phi \approx -6°$. With a latitude of the solar-disk center visible from STEREO-B of $\lambda \approx 2°$, the size of the main CME in the

COR2 images is related to its extent visible from the Earth's direction via the projection factor of $k_{\rm p} = \sin(\theta/2 - \phi')$, where $\phi' \approx \phi - \lambda \approx -8^\circ$. The dashed arcs in Figure 14 calculated from the ballistic kinematics with $\phi' = -7^\circ$ ($k_{\rm p} \approx 0.41$) more or less correspond to the observed size of the main CME.

The flux-rope orientation of $\psi \approx 17^\circ$ suggested by the COR2 images differs from the orientation estimated from the eruption region (42°) by 25°. If this difference really corresponds to the flux-rope rotation, then this amount of rotation was acquired in the CME expansion up to about $20\,{\rm R}_\odot$, as Figure 13 indicates.

The presence of our event in the archive of the WSA – ENLIL + Cone model (*e.g.* Odstrcil, 2003; Mays *et al.*, 2015) at helioweather.net allows comparing our conclusions with the results of numerical modeling. The movies produced by the model show an ICME which was launched on 24 February and corresponds to the main CME. It was directed almost exactly to STEREO-B with the ICME center being slightly displaced to the south–east. Its angular width is close to our estimate of about 35°. This ICME is shown to have reached STEREO-B about half a day later than actually observed that corresponds to the accuracy of the model. These results of the modeling are consistent with our conclusions.

## 4. Interplanetary Transient (ICME)

### 4.1. Magnetic Cloud

The ICME produced by the eruption on 24 February reached STEREO-B on 26 February. No significant disturbance is detectable near Earth until the midday of 28 February. Figure 15 presents *in situ* measurements made by the *Plasma and Suprathermal Ion Composition* (PLASTIC) investigation (Galvin *et al.*, 2008) and by the *Magnetometer* (MAG: Acuña *et al.*, 2008) and the *Solar Wind Electron Analyzer* (SWEA: Sauvaud *et al.*, 2008) of the *In situ Measurements of PArticles and CME Transients* investigation (IMPACT: Luhmann *et al.*, 2008).

The jumps in the proton density and temperature along with a sharp increase in the total magnetic field at 08:20 on 26 February indicate the shock arrival. The following interval until 16:00 shows high density, velocity, temperature, plasma beta, and irregular variations in the total magnetic field that are typical of a sheath region. The MC passage after 16:00 is indicated by low proton density, temperature, plasma beta, and gradual variations of the magnetic field. The pitch-angle distribution of suprathermal electrons in Figure 15f reveals counter-streaming electron flows that indicate a closed MC structure. The velocity jump at the MC front suggests a somewhat faster MC motion within a slower outer layer. A nearly linear trend in the velocity profile in Figure 15b corresponds to a self-similar expansion of the ICME. The plots altogether indicate that the MC passed STEREO-B from 16:00 on 26 February until about 19:00 on 27 February.

Figure 16 presents the magnetic components measured *in situ* in the RTN system along with a proton-velocity plot. The R axis in this system is directed radially outward from Sun, the T axis is roughly tangent to the orbital direction, the N axis is directed northward, and the RN plane contains the solar-rotation axis. The magnetic components fluctuated in the sheath region and became

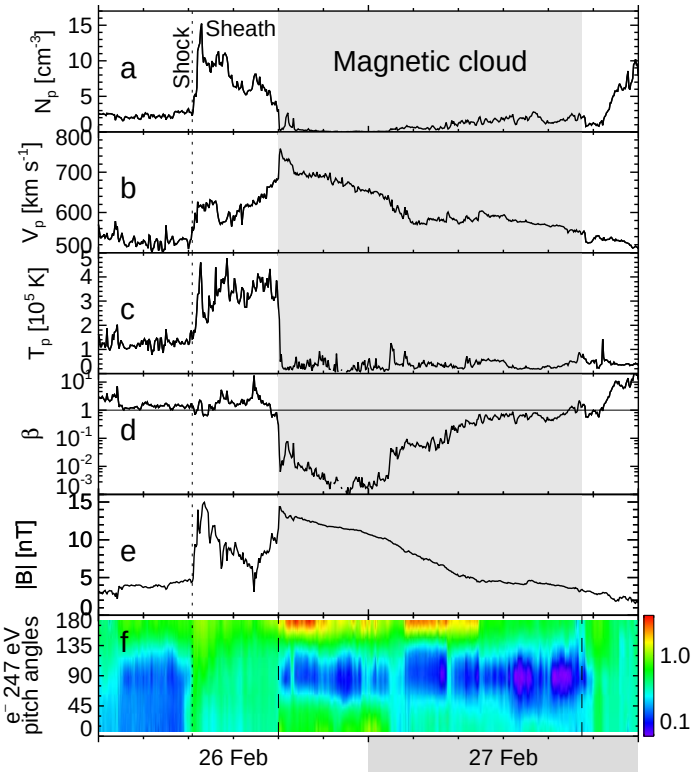


**Figure 15.** ICME produced by the 24 February 2011 event as measured *in situ* on STEREO-B: proton density (**a**), velocity (**b**) and temperature (**c**), plasma beta (**d**), and the magnetic-field magnitude (**e**). Panel **f** presents the pitch-angle distribution of suprathermal electrons quantified by the *color bar* on the right (decimal logarithm of the phase space density (PSD) measured in units of $s^3\,km^{-6}$). The *dotted vertical line* marks the shock arrival. The passage of the magnetic cloud is denoted by the *shading*, and its boundaries on panel **f** are marked by the *dashed vertical lines*. The day numbers are centered at the noon of each date.

smoother in the MC, where their variations mostly agree with the expectations drawn from solar observations in Section 3.5. However, the actual $B_N$ component was only positive that indicates a possible change in the flux-rope orientation.

To find the actual orientation of the MC, we consider a simplest approximation of its magnetic structure with a force-free cylindric flux rope (Lundquist, 1951):

$$B_\rho = 0, \quad B_\varphi = -B_0 J_1(\alpha\rho), \quad B_z = B_0 J_0(\alpha\rho). \tag{2}$$

Here $\rho$, $\varphi$, and $z$ are cylindric coordinates, $B_0$ is a magnetic-field magnitude at the axis of the cylinder, $J_0, J_1$ are the Bessel functions, and $\alpha$ is a force-free constant in the equation $\nabla \times \boldsymbol{B} = \alpha \boldsymbol{B}$. Equation 2 describes a left-handed flux rope in agreement with expectations listed in Section 3.5; a right-handed cylinder contradicts the variations of the magnetic components in Figures 16c – 16e. The value of $\alpha$ is chosen so that $\alpha\rho_0 \approx 2.405$ gives the first zero to $J_0(\alpha\rho_0)$, where $\rho_0$ is the radius of the cylinder. To take account of the flux-rope expansion, the constant values of $[\alpha]$ and $[B_0]$ were replaced with time-dependent quantities

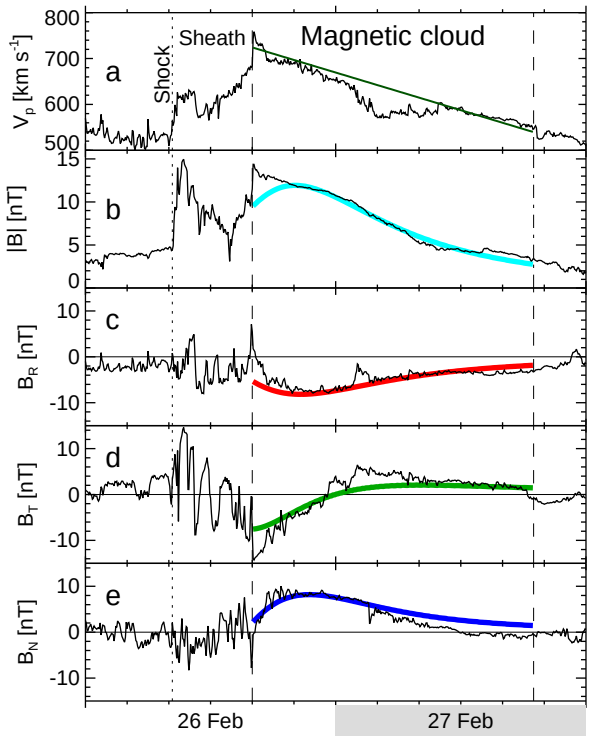


**Figure 16.** *In situ* measurements of the MC on STEREO-B (*black*) and their fit (*thick color curves*): velocity (**a**), the magnitude of the magnetic-field vector (**b**), and its components (**c**, **d**, and **e**) in the RTN system. The *dotted vertical line* marks the shock arrival. The boundaries of the magnetic cloud are denoted by the *dashed vertical lines*.

(Vandas, Romashets, and Geranios, 2015):

$$\alpha \rightarrow \alpha(1 + t/t_0)^{-1}, \quad B_0 \rightarrow B_0(1 + t/t_0)^{-2}, \tag{3}$$

where $t_0$ is the expansion time between the solar eruption and the first contact of the MC with STEREO-B. Equations 3 can also be obtained from considerations of self-similar expansion of an MC with a constant velocity.

The orientation of the MC was searched by an optimization procedure with $\theta^c$, $\phi^c$, $p^c$, and $B_0$ being free parameters. Here $\theta^c$ is the angle between the cylinder-axis and the N axis; $\phi^c$ is the azimuth of the cylinder-axis projection on the RT plane measured from the R axis. Figure 17 illustrates the geometry. The impact parameter $[p^c]$ is the shortest distance between spacecraft and the MC axis in units of $\rho_0$. The situation $p^c = 0$ corresponds to the central collision of the MC with spacecraft. The MC is assumed to expand without rotation self-similarly with a nearly constant velocity throughout its passage at STEREO-B.

The optimization procedure minimizes the standard deviation between the observed magnetic-field temporal profiles $\boldsymbol{B}^{\rm obs}(t_i)$ and the model profiles $\boldsymbol{B}^{\rm mod}(t_i)$

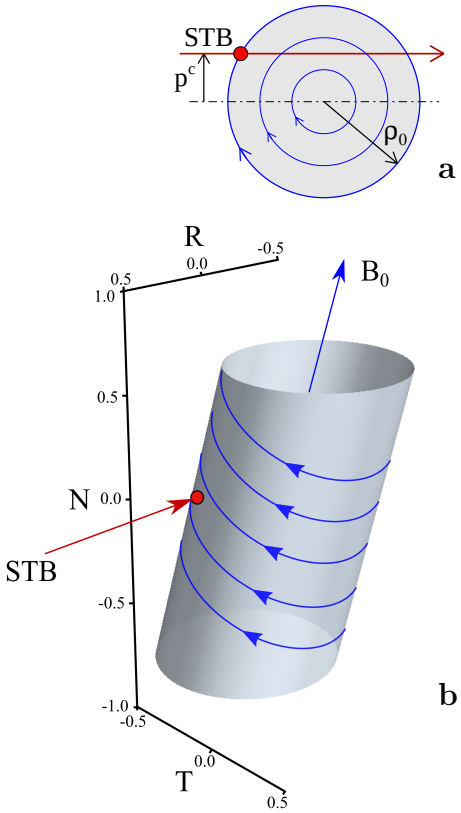


**Figure 17.** The MC orientation found from the modeling of the magnetic components measured *in situ*: (**a**) cross section (top view), (**b**) side view. The axes show the distances from the MC center approximately in units of $2\rho_0$. The MC magnetic structure is schematically presented by the *blue arrows*. The axial $B_z$ component is considered to be zero at the MC surface; the arrows are helical there for clarity. The *brown arrow* indicates the relative motion of STEREO-B with respect to the MC. The *red dot* denotes the site of their first contact.

(Marubashi and Lepping, 2007):

$$\sigma = \sqrt{\frac{1}{N}\sum_{i=0}^{N}\left[\boldsymbol{B}^{\rm obs}(t_i) - \boldsymbol{B}^{\rm mod}(t_i)\right]^2}.$$

The results of the fit are shown in Figures 16b – 16e by the thick color curves. The parameters of the MC found are as follows: $\theta^{\rm c} \approx 15°$, $\phi^{\rm c} \approx 160°$, $p^{\rm c} \approx -0.48$, and $B_0 \approx 15\,{\rm nT}$. The MC arrived at STEREO-B with a small tilt [$\theta^{\rm c}$] to the N axis. Figure 17 shows a sketch of the MC orientation at the STEREO-B position.

To compare the MC orientation with what was expected from solar observations, we converted angles $\theta^{\rm c}$ and $\phi^{\rm c}$ to the coordinates used in Section 3. The angle between the cylinder axis and the Sun–STEREO-B line was $\approx 77°$ that corresponds to the MC direction slightly southward from this line, as Figures 12 and 14 show. Previously we referred to the ecliptic north pole; the solar axis was

inclined to this direction by $\approx 7^\circ$. The estimated angle between the MC axis and this direction was $\psi_{\rm MC} \approx 5^\circ - 7^\circ = -2^\circ$ *vs.* expected $\psi \approx 42^\circ$. The flux-rope orientation suggested by the COR2 observations was $\psi_{\rm COR2} \approx 17^\circ$ (Section 3.6); the flux rope rotated by about 25° close to the Sun. We adopt the total rotation of about 40°; it is not clear if the remaining value is real or a spurious product of our simplified modeling. Indeed, Marubashi *et al.* (2012) pointed out a strong model dependence of the results that the fit of *in situ* measurements provides. Involvement of more complex magnetic-cloud geometries in the modeling (*e.g.* Vandas and Romashets, 2003; Owens *et al.*, 2012) is promising.

We see two possible causes for the counter-clockwise flux-rope rotation. In the first option, large and slow erupting filaments lift off along a neutral surface that combines the neutral lines of the radial magnetic component at different altitudes in the corona (Filippov, Gopalswamy, and Lozhechkin, 2001, 2002; Filippov and Koutchmy, 2008; Grechnev *et al.*, 2014). The magnetic-field extrapolation that we carried out shows that the orientation of the main neutral line changes with an increasing height clockwise and cannot account for the flux-rope rotation.

Another option is a helical bending of the flux-rope axis during eruption. The magnetic configuration in Figure 10 suggests that the axial magnetic field was opposite to the axial electric current. The flux-rope's helical bend develops in this configuration counter-clockwise (*cf.* Figure 2a in Uralov, 1990). This direction corresponds to the flux-rope rotation observed. This process is efficient as long as magnetic field is strong enough and can only occur not far from the Sun.

### 4.2. Ionic Charge State of Iron and Its Evolution

STEREO-B/PLASTIC measured the Fe-ion distribution in the transient. Figure 18a shows the temporal variations of the mean ionic charge state $\langle Q_{\rm Fe}\rangle$ that has two peaks denoted 2 and 3. Figure 18b shows the Fe ionic charge-state distributions observed on 26 February in three regions. Distribution 1 recorded at 12:00 corresponds to the sheath region, where the total density of the Fe ions was highest. Distributions 2 (16:00) and 3 (22:00) present the two peaks of $\langle Q_{\rm Fe}\rangle$ in Figure 18a that correspond to the leading edge of the MC and to its interior. The mean ionic charge state of iron averaged over the whole MC is $\langle Q_{\rm Fe}\rangle = 10.9$.

The mean Fe-ion charge state in the sheath is $\langle Q_{\rm Fe}\rangle = 8.73$ that is a typical value in quasi-stationary solar wind. Both distributions 2 and 3 observed in the MC are bi-modal with $Z \approx 15-17$ in the main peak that represents a hot component and $Z \approx 8-9$ in the minor peak.

To understand the ionic charge state of iron measured on STEREO-B, we numerically simulated the Fe-ion charge state evolution in the CME using the model by Rodkin *et al.* (2017). The model explores the evolution of the Fe-ion charge state in the CME plasma expanding through the corona from the solar source to the "freeze-in" region. We solve the system of continuity equations for a set of Fe ions of interest in the rest frame of the expanding plasma structure taking into account the processes of recombination and ionization. To simulate the Fe ionic charge-state evolution, one needs the temporal variations of the electron temperature and density $[T_{\rm e}(t),\, n_{\rm e}(t)]$ in the moving CME plasma as well as its bulk velocity $[V(t)]$. We related the radial evolution of the bulk velocity

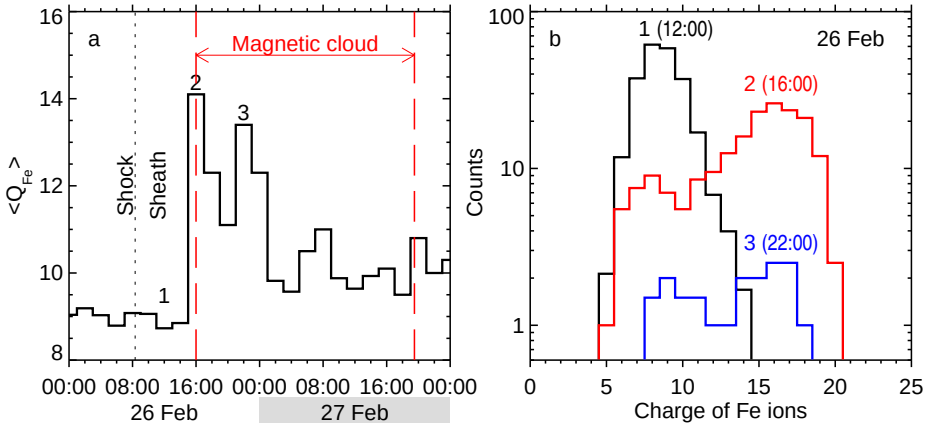


**Figure 18.** STEREO-B/PLASTIC *in situ* measurements of the Fe-ion charge-state distribution. (**a**) Temporal variations of the mean ionic charge state $\langle Q_{\rm Fe}\rangle$ of iron. **b**) Distributions of the Fe ionic charge state in the sheath at 12:00 (*1, black*), in the head of the MC at 16:00 (first peak of $\langle Q_{\rm Fe}\rangle$: *2, red*), and at the second peak of $\langle Q_{\rm Fe}\rangle$ inside the MC (22:00: *3, blue*).

to the kinematic parameters measured for the faster ring in Figure 4b at the heights of $(0.12-0.2)\,{\rm R}_\odot$ above the limb, while no observations are available between $0.2\,{\rm R}_\odot$ and $2\,{\rm R}_\odot$. For certainty and simplicity, we have assigned the velocity at the heights exceeding $0.2\,{\rm R}_\odot$ to the highest velocity of $860\,{\rm km\,s^{-1}}$ that the faster ring reached, as Figure 19a shows.

From the plasma densities and temperatures found in the DEM analysis (Table 1) we evaluated the averaged electron temperatures and densities in moving CME plasma at the heights of $r = (0.12-0.34)\,{\rm R}_\odot$. The plasma parameters for the heights exceeding $0.34\,{\rm R}_\odot$ were extrapolated according to adiabatic expansion conditions. Figures 19b and 19c show the evolution of the electron temperature and density. The number density at a height of $3\,{\rm R}_\odot$ (heliocentric distance of $4\,{\rm R}_\odot$) of $n_{\rm e} = 1.0\times10^6 \lesssim 1.4\times10^6\,{\rm cm^{-3}}$ corresponds to the estimate in Section 3.4 from the parameters of the Type IV burst, whose onset is close to the observation time in Figure 12c, where the CME core reached this distance.

The ions flowing through the corona with solar wind generally have their composition to "freeze-in" within several solar radii from the limb. The freeze-in process depends on the competition between two time scales: the expansion time scale, $\tau_{\rm exp} = n_{\rm e}/(V{\rm d}n_{\rm e}/{\rm d}r)$, which stands for the coronal expansion through the density scale height, and the recombination time scale, $\tau_{\rm rec} = 1/(R_Z n_{\rm e})$ ($R_Z$ is the sum of the radiation and dielectronic recombination rates for the ion of charge $Z$), over which the ions achieve the ionization equilibrium. The electron temperature and density and the plasma velocity are the main physical quantities that determine the ionic charge states in solar wind, and thus the freeze-in process. At the heights, where $\tau_{\rm exp} \ll \tau_{\rm rec}$, the ions achieve frozen-in states. Figure 20 shows the recombination times for the Fe ions used in our analysis in comparison with the expansion time scale calculated with plasma parameters presented in Figure 19. As Figure 20 shows, the ionization state of the $Fe^{8+}-Fe^{14+}$ ions becomes frozen-in at the distances of $r \gtrsim 2\,{\rm R}_\odot$, while that of the $Fe^{15+}-Fe^{23+}$ ions freezes-in earlier, within $2\,{\rm R}_\odot$.

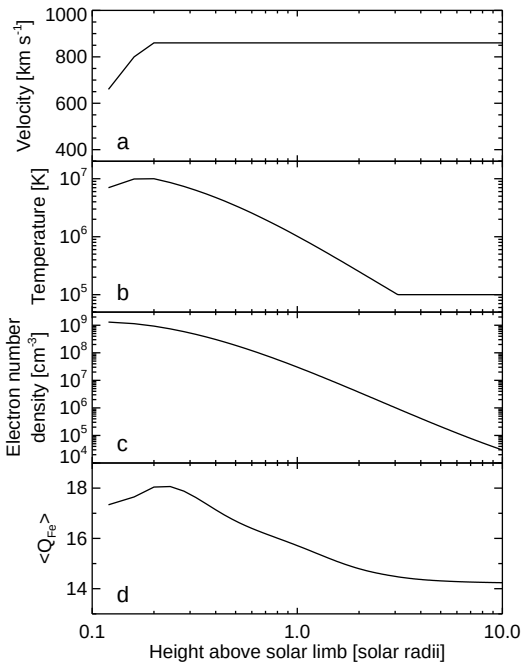


**Figure 19.** Extrapolated parameters of the CME plasma and modeled evolution of the mean charge of iron ions *vs.* the height from the solar limb: velocity (**a**), measured and extrapolated plasma temperature (**b**) and electron number density (**c**), and modeled mean charge of iron ions (**d**).

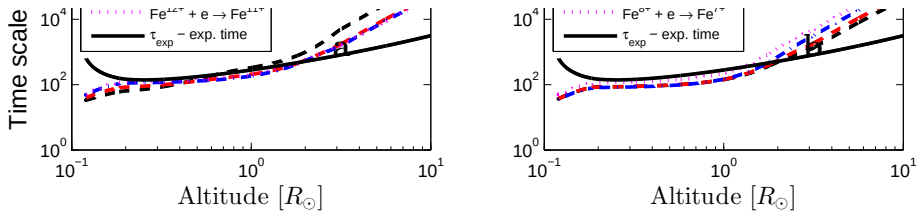


**c** **d**

**Figure 20.** Comparison of the recombination times $\tau_{\rm rec}$ for the Fe ions ($Fe^{8+} - Fe^{23+}$) with the expansion time scale $\tau_{\rm exp}$ (*black dashed curve*).

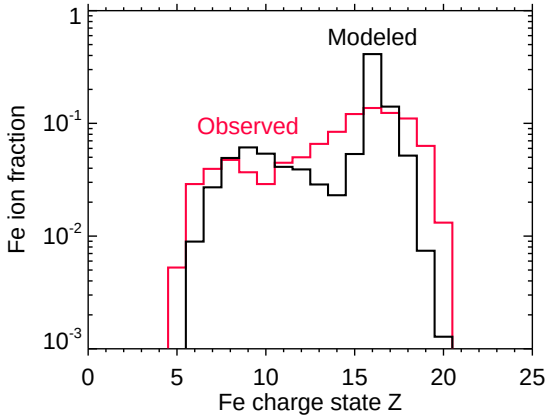


**Figure 21.** Comparison of the modeled frozen-in Fe-ion charge state distribution (*black*) with the distribution actually measured *in situ* by STEREO-B/PLASTIC on 26 February at 16:00 (peak 2: *red*, same as in Figure 18b). The total over each distribution is normalized to unity.

With the plasma parameters presented in Figure 19 we numerically simulated the ionic charge-state evolution of Fe to compare it with the *in situ* measurements. Figure 19d shows the evolution of the average charge of Fe ions $\langle Q_{\rm Fe}\rangle$ from the source region up to a distance of $10\,{\rm R}_\odot$, where the ionic charge state is frozen-in. The modeled freeze-in value $\langle Q_{\rm Fe}\rangle = 14.24$ is close to the measured $\langle Q_{\rm Fe}\rangle = 14.16$. Figure 21 compares the simulated Fe-ion charge-state distribution with distribution 2 in Figure 18b observed *in situ* on 26 February at 16:00. The simulation renders the main features of the actual distribution, in particular its bi-modal character with the peaks around the $Fe^{9+}$ and $Fe^{16+}$ charge states. Distribution 3 observed at 22:00 had similar properties. Our results agree with a conclusion of Lynch *et al.* (2011) that the cause of enhanced heavy-ion charge states in CMEs is flare heating in the low corona.

Bi-modal Fe charge-state distributions observed *in situ* are usually interpreted by mixing between hot and cold components of solar wind. Conversely, Gruesbeck *et al.* (2011) proposed that the bi-modality of the Fe-ion distribution could result from rapid plasma heating at a high initial density near the Sun with subsequent cooling caused by the rapid plasma expansion and thus may be an intrinsic property of the CME plasma. The results of our modeling agree with this conclusion. Furthermore, the bi-modality of the Fe-ion distribution can be caused by the fact that the $Fe^{16+}$ – $Fe^{18+}$ ions have recombination rates considerably lower than the $Fe^{14+}$ and $Fe^{15+}$ ions, and therefore the former freeze-in earlier.

An approximate generalized analysis in Section A (Appendix) confirms the results of the modeling and shows that the properties of the ionic charge state of iron obtained in this section can be expected for fast CMEs.

### 4.3. CME/ICME Propagation

Some parts of the interplanetary transient can be identified with their solar progenitors due to *i*) kinematics measured for the erupting prominence and CME, *ii*) identification of the MC with its solar source, and *iii*) analysis of

the charge state of Fe ions that marks hot plasma. The two rings of the erupted prominence strongly accelerated and heated up to $10^7$ K. The rings kinematically correspond to the CME core. The magnetic structure of the ICME corresponds to its solar source. The charge state of Fe ions measured in the head of the MC corresponds to the temperature of the heated prominence, which for these reasons was the most probable progenitor of the CME core and MC.

The arrival time of the MC at 16:00 on 26 February (peak 2 in Figure 18) corresponds within the uncertainties to the estimate for the ballistic motion of the CME core in Figure 13. The velocity of the MC front in Figure 16a is comparable with the expected $706\,\mathrm{km\,s^{-1}}$. The proton velocity at 22:00 (peak 3) was $\approx 675\,\mathrm{km\,s^{-1}}$. From Equation 1 we estimate a corresponding velocity $v_0 = 735\,\mathrm{km\,s^{-1}}$ at a distance $r_0 = 4.5\,\mathrm{R_\odot}$ and transit time from $r_0$ to STEREO-B at $r_1 = 1.02$ AU of 61.25 hours. At a corresponding time of 08:45 on 24 February, the LASCO-C2 movies in the CME catalog (cdaw.gsfc.nasa.gov/CME_list/) reveal an ejection with a leading edge at a few solar radii. The velocity of $v_0 = 735\,\mathrm{km\,s^{-1}}$ seems to be consistent with its motion, being close to an average velocity of this ejection, if its source was the secondary eruption around 07:53.

Thus, the solar source of peak 2 in the Fe-ion charge-state distribution in Figure 18 was the main eruption around 07:30; the source of peak 3 might be the eruption around 07:53. Both hot signatures located in the MC appear to have moved from the Sun to the STEREO-B orbit ballistically. On the other hand, the initial speed of the CME leading edge $v_0 > 1100\,\mathrm{km\,s^{-1}}$ considerably exceeded the solar-wind speed $v_{SW} < 660\,\mathrm{km\,s^{-1}}$, so that strong drag was expected for the nose of the transient. The fact that the CME core was considerably slower than its leading edge in Figure 12 indicates that the CME core (MC) might not have occupied the whole cavity, being separated from the nose of the transient by a gap. This probable gap (part of cavity) was presumably softer than the MC, being initially filled with low-density plasma, while magnetic field in the gap was weaker than in the MC (see Figure 15e).

The interplanetary transient was probably inhomogeneous: *i*) The CME core (MC) was surrounded by a thick layer in the cavity bounded by the frontal structure; *ii*) The velocity jump at the MC front at 16:00 on 26 February in Figure 15b suggests that the faster MC moved in a slower environment, while the latter moved in the solar wind, which was still slower. The drag force acted on the front of the softer outer layer in the gap that could reduce the pressure of the upstream solar wind applied to the MC. The outer layer was probably compressed and partly extruded, flowing around the MC.

To specify this scenario, we modeled the CME/ICME front propagation using the online Drag-Based Model at oh.geof.unizg.hr/DBM/dbm.php (Vršnak *et al.*, 2013). With a drag parameter $\Gamma = (3.5 - 4.5) \times 10^{-8}\,\mathrm{km^{-1}}$ and actual CME speed, the model provides realistic velocities and the front arrival time slightly ahead of the MC. While the core/MC somewhat decelerates within $20\,\mathrm{R_\odot}$ from the Sun, the front velocity decreases down to the MC velocity at $\approx 0.5$ AU and goes on decreasing afterwards. The distance between the front and core/MC (*i.e.* the width of the gap) increases up to $\approx 0.1$ AU at $\approx 0.5$ AU and then decreases to $\approx 0.05$ AU at the STEREO-B orbit that corresponds to the compression of the gap. Thus, the ballistic MC kinematics is compatible with the presence of a considerable drag.

## 5. Summary and Concluding Remarks

Using remote observations and *in situ* measurements, we followed the history of an interplanetary transient from the solar eruption on 24 February 2011, where it originated, up to the STEREO-B orbit. We identified some parts of the interplanetary transient with their solar progenitors due to magnetic structures that were revealed in the ICME and its solar source, kinematical measurements, and marks of high-temperature regions. The analysis of observations is supplemented and elaborated by modeling and theoretical considerations. In particular, the "frozen-in" charge-state distribution of Fe ions in CME plasma was modeled, invoking the ionization/recombination balance equations and using as input parameters the electron temperatures and densities estimated from observations. Numerical simulations reproduced both the average charge $\langle Q_{\rm Fe}\rangle$ and the charge-state distribution of Fe ions observed *in situ*. The results are as follows:

i) The flux-rope progenitor was formed from magnetic structures of the eruptive prominence and inherited its plasma. Then the flux-rope progenitor became the CME core and, eventually, the magnetic cloud.

ii) The eruptive prominence underwent two stages of heating. It was heated at the initiation stage presumably by electric currents. The brightness of the prominence corresponded at this stage to an increasing soft X-ray flux (Figure 8). The pre-eruptive heating considerably increased the pressure in the prominence that could be significant in driving the sharp eruption.

   The erupting prominence transformed into curled ring-like structures, which pushed long loops ahead. The eruption started first, and then the flare emission appeared. During the flare impulsive phase, the brightness of the erupting prominence correlated with a hard X-ray flux (Figure 9). The erupting structures were presumably heated up to about 10 MK by accelerated electrons injected from the reconnection site. Electrons trapped in the erupting structures probably produced a Type IV burst.

iii) The model demonstrates that a large fraction of Fe ions with a charge state $\geq 16^+$ in our ICME was produced due to both strong heating in the erupting structure and high CME velocity reached at the early stage of expansion. The modeling also shows that the bi-modality of the Fe-ion charge-state distribution frequently observed in ICMEs may be their intrinsic property. The bi-modal distribution which forms during the CME/ICME expansion can in these cases be accounted for by different recombination rates for low and high charge states of Fe. The high ionic charge-state of Fe in the magnetic cloud certifies its association with the heated erupting prominence.

iv) The ICME magnetic structure inherited properties of its solar progenitor, being therefore predictable. The flux rope rotated by $\approx 40^\circ$ not far from the Sun that was detected from coronagraph observations.

v) The motion of the flux rope from the Sun to the STEREO-B orbit appears to be ballistic, while the nose of the interplanetary transient was probably influenced by the drag force from the upstream solar wind. These circumstances indicate that a gap in between underwent compression.

Our case study of the SOL2011-02-24 event has shown that several parameters of an ICME near the Earth orbit are determined by the solar eruption, which produced it, and can be estimated from solar observations. Our study indicates that internal structures of a CME and not only its outer boundary deserve attention. We hope that our results can be helpful in elaborating the models of the CME formation and propagation in the interplanetary space.

**Acknowledgments** We thank D.V. Prosovetsky, Yu.S. Shugay, B.V. Somov, and A.V. Kiselev for their assistance and discussions. We are indebted to the co-authors of the Grechnev *et al.* (2015) article that provided the basis for the present work. We thank the anonymous reviewer for valuable remarks.

V. Slemzin and D. Rodkin (Sections 2, 3.3, and 4.2) were funded by the Russian Science Foundation (RSF) under grant 17-12-01567. V. Grechnev, A. Kochanov, A. Uralov, V. Kiselev, and I. Myshyakov (Sections 3.1, 3.2, 3.4 – 3.6, 4.1, 4.3, and Section A) were funded by the RSF under grant 18-12-00172.

We thank the NASA/SDO and the AIA and HMI science teams; the NASA's STEREO/SECCHI science and instrument teams; the teams operating RHESSI, SOHO/LASCO, S/WAVES, and the GOES satellites for the data used here. SOHO is a project of international cooperation between ESA and NASA. We are grateful to the team maintaining the CME Catalog at the CDAW Data Center by NASA and the Catholic University of America in cooperation with the Naval Research Laboratory. We thank the team that created and maintains the online archive of the WSA – ENLIL + Cone Model and the team that created the online Drag-Based Model.

## Disclosure of Potential Conflicts of Interest

The authors declare that they have no conflicts of interest.

## Appendix

## A. General Expectations for the Fe-ion Charge State

Figure 20 shows that the freeze-in process for the Fe-ion charge state starts within $1\,\mathrm{R}_\odot$ for higher-charge ions and at $\gtrsim 2\,\mathrm{R}_\odot$ for lower-charge ions. The freeze-in distance $r_{\mathrm{fr}}$ is determined by the kinematics and plasma parameters of a structure propagating through the corona. To derive an analytical expression for $r_{\mathrm{fr}}$ and its dependence on the parameters of an eruptive event, the plasma expansion timescale $\tau_{\mathrm{exp}}$ should be compared with recombination time $\tau_{\mathrm{rec}}$.

The expansion timescale is $\tau_{\mathrm{exp}} = n_{\mathrm{e}}/|\mathrm{d}n_{\mathrm{e}}/\mathrm{d}t|$, where $\mathrm{d}n_{\mathrm{e}}/\mathrm{d}t = \partial n_{\mathrm{e}}/\partial t + (\boldsymbol{V}\cdot\nabla)n_{\mathrm{e}}$. In stationary solar wind $\partial/\partial t = 0$. In our case $\partial/\partial t \neq 0$ and $\tau_{\mathrm{exp}}$ depends on deformation of the moving plasma volume. For self-similar expansion $n_{\mathrm{e}} = n_0(r_0/r)^3$, where $r$ is a distance from the eruption center that is located near the solar surface, and $r_0$ is a distance where the adiabatic regime starts. It follows from these expressions that $|\mathrm{d}n_{\mathrm{e}}/\mathrm{d}t| = n_{\mathrm{e}}(3V/r)$, where $V = \mathrm{d}r/\mathrm{d}t$ is the

velocity of the leading edge of the erupting structure. For $r \geq r_0$, the velocity is assumed to be constant ($V = V_0$) and the expansion timescale is

$$\tau_{\rm exp} = \tau_{0\,\rm exp}(r/r_0), \quad \text{where } \tau_{0\,\rm exp} = r_0/3V_0. \tag{4}$$

The total recombination rate for the ion with a charge $Z$ is $R_Z = R_{\rm di} + R_{\rm rad}$ ($\rm cm^3\,sec^{-1}$), where $R_{\rm di}$ and $R_{\rm rad}$ are the dielectronic and radiative recombination rates, respectively. To estimate the dependence $\tau_{\rm rec}(r)$ at temperatures of ($10^6$ – $10^8$) K, we only consider the dielectronic recombination contribution $R_{\rm di}$, which usually prevails at high temperatures. With the plasma parameters in Figure 19, these temperatures correspond to the distances $r \leq 1\,\rm R_\odot$. For the dielectronic recombination rate we use Equation 7 from Arnaud and Raymond (1992):

$$R_{\rm di}(T_{\rm e}) = T_{\rm e}^{-3/2} \sum c_i \exp(-E_i/kT_{\rm e})\,\rm cm^3\,s^{-1},$$

where $T_{\rm e}$ is in K, $kT_{\rm e}$ and $E_i$ are in eV, and $c_i$ is in $\rm cm^3\,s^{-1}\,K^{1.5}$. The values of $E_i$ and $c_i$ are tabulated. The adiabatic plasma cooling for $r > r_0$ and $T_{\rm e} = T_0(n_{\rm e}/n_0)^{\gamma-1} = T_0(r/r_0)^{-3(\gamma-1)}$ results in a recombination time

$$\tau_{\rm rec}^{-1} \approx \tau_{\rm di}^{-1} = n_{\rm e} R_{\rm di} = n_0 T_0^{-3/2} (r/r_0)^{4.5(\gamma-5/3)} \sum c_i (\varepsilon_{0\,i})^{f''},$$

where $\gamma$ is the adiabatic index, $\varepsilon_{0\,i} = \exp(-E_i/kT_0)$, and $f'' = (r/r_0)^{3(\gamma-1)}$. The terms summed stand for atomic physics of the recombination process, and the product $n_{\rm e}T_{\rm e}^{-3/2}$ is proportional to the Coulomb collision frequency $\nu_{\rm ie}$ of an ion with thermal electrons. For $\gamma = 5/3$ we obtain

$$\tau_{\rm di}^{-1} = n_0 T_0^{-3/2} \sum c_i (\varepsilon_{0\,i})^{f}, \quad f = (r/r_0)^2.$$

To estimate the recombination time $\tau_{\rm di}$, we consider the $Fe^{16+}$ ion that is one of the first ions undergoing the freeze-in process (Figure 20). For this ion the sum $\sum c_i(\varepsilon_{0\,i})^f$ is reduced to a single term $c_1 = 1.23$, $E_1 = 560\,\rm eV$, $\varepsilon_{01} = \exp(-560\,\rm eV/kT_0)$ (Arnaud and Raymond, 1992). Thus,

$$\tau_{\rm di} = \tau_{0\,\rm di}(\varepsilon_{01})^{1-f}, \quad \tau_{0\,\rm di} = T_0^{3/2}/(n_0 c_1 \varepsilon_{01}). \tag{5}$$

The freeze-in distance is determined by the competition between the expansion and recombination timescales that we characterize by a ratio $m = \tau_{\rm rec}/\tau_{\rm exp}$. The complete frozen-in situation corresponds to $m \gg 1$. To estimate the freeze-in distance $r_{\rm fr}$, we use the relation $m\tau_{\rm exp} = \tau_{\rm rec} \approx \tau_{\rm di}$ with $m = 3$. The usage of Equations 4 and 5 in this relation yields

$$\mu^{0.5}\varepsilon_{01}^{\mu} = \varepsilon_{01}\,\tau_{0\,\rm di}/(m\tau_{0\,\rm exp}) = 3V_0T_0^{3/2}/(mr_0n_0c_1) \quad \text{with } \mu = (r_{\rm fr}/r_0)^2. \tag{6}$$

We apply Equation 6 to our event, whose parameters are shown in Section 4.2. Taking the electron density and temperature at $r_0 = 0.34\,\rm R_\odot$ to be $n_0 = 10^9\,\rm cm^{-3}$ and $T_0 = 11.6 \times 10^6\,\rm K$ ($kT_0 = 1\,\rm keV$), and $V_0 = 860\,\rm km\,s^{-1}$, we get $\varepsilon_{01} = \exp(-0.56) = 0.67$ and $\tau_{0\,\rm di} = 46\,\rm s$. With $m = 3$, Equation 6 takes a

form $\mu^{0.5}0.67^{\mu} = 0.11$; thus, $\mu^{0.5} = r_{\rm fr}/r_0 \approx 2.85$ and $r_{\rm fr} \approx 2.85 r_0 \approx 0.97\,{\rm R}_\odot$. As follows from Section 4.2, ions $Fe^{16+}$ freeze-in earlier than the mean charge $\langle Q_{\rm Fe}\rangle$, whose variations are shown in Figure 19d. The main decrease in $\langle Q_{\rm Fe}\rangle$ occurs within $r < r_{\rm fr}$. Note that the solutions of Equation 6 for $m = 2$ and $m = 1$ are the values $r_{\rm fr} \approx 2.6 r_0 \approx 0.88\,{\rm R}_\odot$ and $r_{\rm fr} \approx 2.15 r_0 \approx 0.73\,{\rm R}_\odot$, respectively. The latter value is not much different from $r \approx 0.5\,{\rm R}_\odot$ where the curves $\tau_{\rm exp}$ and $\tau_{\rm rec}$ in Figure 20 calculated for $Fe^{16+}$ intersect. The results obtained from Equation 6 are reasonably close to the numerical calculations presented in Section 4.2.

For generalized estimates, Equation 6 can be simplified by replacing the $r_0/V_0$ ratio with $\tau_{\rm acc}/2$, where $\tau_{\rm acc}$ is a characteristic time, when an eruption moving with an effective constant acceleration $[a]$ reaches the velocity $V_0 = a\tau_{\rm acc}$; $r_0 = a\tau_{\rm acc}^2/2$. This estimate of $r_0$ implies the plasma heating only at the acceleration stage of the erupting filament. For a typical $\tau_{\rm acc} \approx 300\,{\rm s}$ and $V_0 \approx 10^3\,{\rm km\,s^{-1}}$ in eruptions from active regions we estimate $r_0 \approx 0.2\,{\rm R}_\odot$, which is slightly different from $r_0 \approx 0.34\,{\rm R}_\odot$ obtained in the numerical modeling of the charge-state evolution in Section 4.2. With $m = 3$, Equation 6 transforms to a form

$$\mu^{0.5}(\varepsilon_{01})^{\mu} \approx 2T_0^{3/2}/(c_1 n_0 \tau_{\rm acc}) \propto (\tau_{\rm acc}\nu_{0\,{\rm ie}})^{-1} \quad \text{with } \nu_{0\,{\rm ie}} = \nu_{\rm ie}\,(r = r_0). \qquad (7)$$

The right part of this equation does not contain $r_0$, unlike Equation 6. Calculations show that an increase in the right parts of Equations 6 and 7 corresponds to a decrease in the $r_{\rm fr}/r_0$ ratio. Case studies of eruptions from active regions show that their temperatures at the acceleration stage reach $\approx 10^7\,{\rm K}$ ($kT_0 \approx 1\,{\rm keV}$; *e.g.* Glesener *et al.*, 2013; Grechnev *et al.*, 2016). For $n_0 = 10^9\,{\rm cm^{-3}}$ Equation 7 yields $\mu^{0.5}0.67^{\mu} \approx 0.22$, $r_{\rm fr}/r_0 \approx 2.45$, and $r_{\rm fr} \approx 0.5\,{\rm R}_\odot$. The dependence on $n_0$ is weak; with $n_0 = 10^{10}\,{\rm cm^{-3}}$ and other parameters unchanged, $r_{\rm fr} \approx 0.7\,{\rm R}_\odot$.

Thus, the high ionic charge states of iron are expected to form in fast CMEs near the Sun and not to change afterwards considerably. This conclusion is consistent with the results of the numerical calculations by Rodkin *et al.* (2017).

## References


Acuña, M.H., Curtis, D., Scheifele, J.L., Russell, C.T., Schroeder, P., Szabo, A., Luhmann, J.G.: 2008, The STEREO/IMPACT magnetic field experiment. *Space Sci. Rev.* **136**, 203. DOI. ADS.

Amari, T., Luciani, J.F., Mikic, Z., Linker, J.: 2000, A twisted flux rope model for coronal mass ejections and two-ribbon flares. *Astrophys. J. Lett.* **529**, L49. DOI. ADS.

Anzer, U.: 1978, Can coronal loop transients be driven magnetically? *Solar Phys.* **57**, 111. DOI. ADS.

Anzer, U., Heinzel, P.: 2005, On the nature of dark extreme ultraviolet structures seen by SOHO/EIT and TRACE. *Astrophys. J.* **622**, 714. DOI. ADS.

Arnaud, M., Raymond, J.: 1992, Iron ionization and recombination rates and ionization equilibrium. *Astrophys. J.* **398**, 394. DOI. ADS.

Aschwanden, M.J., Gopalswamy, N.: 2019, Global energetics of solar flares. VII. Aerodynamic drag in coronal mass ejections. *Astrophys. J.* **877**, 149. DOI. ADS.

Battaglia, M., Kontar, E.P.: 2012, RHESSI and SDO/AIA observations of the chromospheric and coronal plasma parameters during a solar flare. *Astrophys. J.* **760**, 142. DOI. ADS.

Bougeret, J.L., Goetz, K., Kaiser, M.L., Bale, S.D., Kellogg, P.J., Maksimovic, M., Monge, N., Monson, S.J., Astier, P.L., Davy, S., *et al.*: 2008, S/WAVES: The Radio and Plasma Wave Investigation on the STEREO mission. *Space Sci. Rev.* **136**, 487. DOI. ADS.

Brueckner, G.E., Howard, R.A., Koomen, M.J., Korendyke, C.M., Michels, D.J., Moses, J.D., Socker, D.G., Dere, K.P., Lamy, P.L., Llebaria, A., *et al.*: 1995, The Large Angle Spectroscopic Coronagraph (LASCO). *Solar Phys.* **162**, 357. DOI. ADS.

Canfield, R.C., Hudson, H.S., McKenzie, D.E.: 1999, Sigmoidal morphology and eruptive solar activity. *Geophys. Res. Lett.* **26**, 627. DOI. ADS.

Cargill, P.J.: 2004, On the aerodynamic drag force acting on interplanetary coronal mass ejections. *Solar Phys.* **221**, 135. DOI. ADS.

Chen, J.: 1989, Effects of toroidal forces in current loops embedded in a background plasma. *Astrophys. J.* **338**, 453. DOI. ADS.

Chen, J.: 1996, Theory of prominence eruption and propagation: Interplanetary consequences. *J. Geophys. Res.* **101**, 27499. DOI. ADS.

Chen, J.: 2017, Physics of erupting solar flux ropes: Coronal mass ejections (CMEs)—Recent advances in theory and observation. *Phys. Plasmas* **24**, 090501. DOI. ADS.

Chen, J., Krall, J.: 2003, Acceleration of coronal mass ejections. *J. Geophys. Res.* **108**, 1410. DOI. ADS.

Chertok, I.M., Grechnev, V.V., Abunin, A.A.: 2017, An early diagnostics of the geoeffectiveness of solar eruptions from photospheric magnetic flux observations: the transition from SOHO to SDO. *Solar Phys.* **292**, 62. DOI. ADS.

Chertok, I.M., Grechnev, V.V., Belov, A.V., Abunin, A.A.: 2013, Magnetic flux of EUV arcade and dimming regions as a relevant parameter for early diagnostics of solar eruptions – sources of non-recurrent geomagnetic storms and Forbush decreases. *Solar Phys.* **282**, 175. DOI. ADS.

Démoulin, P.: 2010, Interaction of ICMEs with the solar wind. In: Maksimovic, M., Issautier, K., Meyer-Vernet, N., Moncuquet, M., Pantellini, F. (eds.) *Twelfth International Solar Wind Conference*, *American Institute of Physics Conference Series* **1216**, 329. DOI. ADS.

Démoulin, P., Aulanier, G.: 2010, Criteria for flux rope eruption: Non-equilibrium versus torus instability. *Astrophys. J.* **718**, 1388. DOI. ADS.

Domingo, V., Fleck, B., Poland, A.I.: 1995, The SOHO mission: an overview. *Solar Phys.* **162**, 1. DOI. ADS.

Filippov, B.: 2013, Electric current equilibrium in the corona. *Solar Phys.* **283**, 401. DOI. ADS.

Filippov, B., Koutchmy, S.: 2008, Causal relationships between eruptive prominences and coronal mass ejections. *Ann. Geophys.* **26**, 3025. DOI. ADS.

Filippov, B.P., Gopalswamy, N., Lozhechkin, A.V.: 2001, Non-radial motion of eruptive filaments. *Solar Phys.* **203**, 119. DOI. ADS.

Filippov, B.P., Gopalswamy, N., Lozhechkin, A.V.: 2002, Motion of an eruptive prominence in the solar corona. *Astron. Rep.* **46**, 417. DOI. ADS.

Foullon, C., Owen, C.J., Dasso, S., Green, L.M., Dandouras, I., Elliott, H.A., Fazakerley, A.N., Bogdanova, Y.V., Crooker, N.U.: 2007, Multi-spacecraft study of the 21 January 2005 ICME. Evidence of current sheet substructure near the periphery of a strongly expanding, fast magnetic cloud. *Solar Phys.* **244**, 139. DOI. ADS.

Galvin, A.B., Kistler, L.M., Popecki, M.A., Farrugia, C.J., Simunac, K.D.C., Ellis, L., Möbius, E., Lee, M.A., Boehm, M., Carroll, J., *et al.*: 2008, The Plasma and Suprathermal Ion Composition (PLASTIC) investigation on the STEREO observatories. *Space Sci. Rev.* **136**, 437. DOI. ADS.

Gibson, S.E., Low, B.C.: 1998, A time-dependent three-dimensional magnetohydrodynamic model of the coronal mass ejection. *Astrophys. J.* **493**, 460. DOI. ADS.

Glesener, L., Krucker, S., Bain, H.M., Lin, R.P.: 2013, Observation of heating by flare-accelerated electrons in a solar coronal mass ejection. *Astrophys. J. Lett.* **779**, L29. DOI. ADS.

Gopalswamy, N., Yashiro, S., Akiyama, S., Xie, H.: 2017, Estimation of reconnection flux using post-eruption arcades and its relevance to magnetic clouds at 1 AU. *Solar Phys.* **292**, 65. DOI. ADS.

Grechnev, V.V., Chertok, I.M., Slemzin, V.A., Kuzin, S.V., Ignat'ev, A.P., Pertsov, A.A., Zhitnik, I.A., Delaboudinière, J.-P., Auchère, F.: 2005, CORONAS-F/SPIRIT EUV observations of October-November 2003 solar eruptive events in combination with SOHO/EIT data. *J. Geophys. Res.* **110**, A09S07. DOI. ADS.

Grechnev, V.V., Uralov, A.M., Zandanov, V.G., Baranov, N.Y., Shibasaki, K.: 2006, Observations of prominence eruptions with two radioheliographs, SSRT, and NoRH. *Publ. Astron. Soc. Japan* **58**, 69. DOI. ADS.

Grechnev, V.V., Kuz'menko, I.V., Uralov, A.M., Chertok, I.M., Kochanov, A.A.: 2013, Microwave negative bursts as indications of reconnection between eruptive filaments and a large-scale coronal magnetic environment. *Publ. Astron. Soc. Japan* **65**, S10. DOI. ADS.

Grechnev, V.V., Uralov, A.M., Slemzin, V.A., Chertok, I.M., Filippov, B.P., Rudenko, G.V., Temmer, M.: 2014, A challenging solar eruptive event of 18 November 2003 and the causes of the 20 November geomagnetic superstorm. I. Unusual history of an eruptive filament. *Solar Phys.* **289**, 289. DOI. ADS.

Grechnev, V.V., Uralov, A.M., Kuzmenko, I.V., Kochanov, A.A., Chertok, I.M., Kalashnikov, S.S.: 2015, Responsibility of a filament eruption for the initiation of a flare, CME, and blast wave, and its possible transformation into a bow shock. *Solar Phys.* **290**, 129. DOI. ADS.

Grechnev, V.V., Uralov, A.M., Kochanov, A.A., Kuzmenko, I.V., Prosovetsky, D.V., Egorov, Y.I., Fainshtein, V.G., Kashapova, L.K.: 2016, A tiny eruptive filament as a flux-rope progenitor and driver of a large-scale CME and wave. *Solar Phys.* **291**, 1173. DOI. ADS.

Gruesbeck, J.R., Lepri, S.T., Zurbuchen, T.H., Antiochos, S.K.: 2011, Constraints on coronal mass ejection evolution from in situ observations of ionic charge states. *Astrophys. J.* **730**, 103. DOI. ADS.

Howard, R.A., Moses, J.D., Vourlidas, A., Newmark, J.S., Socker, D.G., Plunkett, S.P., Korendyke, C.M., Cook, J.W., Hurley, A., Davila, J.M., *et al.*: 2008, Sun Earth Connection Coronal and Heliospheric Investigation (SECCHI). *Space Sci. Rev.* **136**, 67. DOI. ADS.

James, A.W., Green, L.M., Palmerio, E., Valori, G., Reid, H.A.S., Baker, D., Brooks, D.H., van Driel-Gesztelyi, L., Kilpua, E.K.J.: 2017, On-disc observations of flux rope formation prior to its eruption. *Solar Phys.* **292**, 71. DOI. ADS.

Jian, L.K., MacNeice, P.J., Taktakishvili, A., Odstrcil, D., Jackson, B., Yu, H.-S., Riley, P., Sokolov, I.V., Evans, R.M.: 2015, Validation for solar wind prediction at Earth: Comparison of coronal and heliospheric models installed at the CCMC. *Space Weather* **13**, 316. DOI.

Kaiser, M.L., Kucera, T.A., Davila, J.M., St. Cyr, O.C., Guhathakurta, M., Christian, E.: 2008, The STEREO mission: an introduction. *Space Sci. Rev.* **136**, 5. DOI. ADS.

Kumar, P., Cho, K.-S., Bong, S.-C., Park, S.-H., Kim, Y.H.: 2012, Initiation of coronal mass ejection and associated flare caused by helical kink instability observed by SDO/AIA. *Astrophys. J.* **746**, 67. DOI. ADS.

Landi, E., Raymond, J.C., Miralles, M.P., Hara, H.: 2010, Physical conditions in a coronal mass ejection from Hinode, STEREO, and SOHO observations. *Astrophys. J.* **711**, 75. DOI. ADS.

Lee, J.-Y., Raymond, J.C., Ko, Y.-K., Kim, K.-S.: 2009, Three-dimensional structure and energy balance of a coronal mass ejection. *Astrophys. J.* **692**, 1271. DOI. ADS.

Lemen, J.R., Title, A.M., Akin, D.J., Boerner, P.F., Chou, C., Drake, J.F., Duncan, D.W., Edwards, C.G., Friedlaender, F.M., Heyman, G.F., *et al.*: 2012, The Atmospheric Imaging Assembly (AIA) on the Solar Dynamics Observatory (SDO). *Solar Phys.* **275**, 17. DOI. ADS.

Lepri, S.T., Zurbuchen, T.H.: 2004, Iron charge state distributions as an indicator of hot ICMEs: Possible sources and temporal and spatial variations during solar maximum. *J. Geophys. Res.* **109**, A01112. DOI. ADS.

Lepri, S.T., Zurbuchen, T.H., Fisk, L.A., Richardson, I.G., Cane, H.V., Gloeckler, G.: 2001, Iron charge distribution as an identifier of interplanetary coronal mass ejections. *J. Geophys. Res.* **106**, 29231. DOI. ADS.

Lin, C.-H., Gallagher, P.T., Raftery, C.L.: 2010, Investigating the driving mechanisms of coronal mass ejections. *Astron. Astrophys.* **516**, A44. DOI. ADS.

Lin, R.P., Dennis, B.R., Hurford, G.J., Smith, D.M., Zehnder, A., Harvey, P.R., Curtis, D.W., Pankow, D., Turin, P., Bester, M., *et al.*: 2002, The Reuven Ramaty High-Energy Solar Spectroscopic Imager (RHESSI). *Solar Phys.* **210**, 3. DOI. ADS.

Liu, Y., Davies, J.A., Luhmann, J.G., Vourlidas, A., Bale, S.D., Lin, R.P.: 2010, Geometric triangulation of imaging observations to track coronal mass ejections continuously out to 1 AU. *Astrophys. J. Lett.* **710**, L82. DOI. ADS.

Low, B.C.: 1982, Self-similar magnetohydrodynamics. I – The gamma = 4/3 polytrope and the coronal transient. *Astrophys. J.* **254**, 796. DOI. ADS.

Luhmann, J.G., Curtis, D.W., Schroeder, P., McCauley, J., Lin, R.P., Larson, D.E., Bale, S.D., Sauvaud, J.-A., Aoustin, C., Mewaldt, R.A., *et al.*: 2008, STEREO IMPACT investigation goals, measurements, and data products overview. *Space Sci. Rev.* **136**, 117. DOI. ADS.

Lundquist, S.: 1951, On the stability of magneto-hydrostatic fields. *Phys. Rev.* **83**, 307. DOI. ADS.

Lynch, B.J., Reinard, A.A., Mulligan, T., Reeves, K.K., Rakowski, C.E., Allred, J.C., Li, Y., Laming, J.M., MacNeice, P.J., Linker, J.A.: 2011, Ionic composition structure of coronal mass ejections in axisymmetric magnetohydrodynamic models. *Astrophys. J.* **740**, 112. DOI. ADS.

Manchester, W.B. IV, Vourlidas, A., Tóth, G., Lugaz, N., Roussev, I.I., Sokolov, I.V., Gombosi, T.I., De Zeeuw, D.L., Opher, M.: 2008, Three-dimensional MHD simulation of the 2003 October 28 coronal mass ejection: Comparison with LASCO coronagraph observations. *Astrophys. J.* **684**, 1448. DOI. ADS.

Manchester, W., Kilpua, E.K.J., Liu, Y.D., Lugaz, N., Riley, P., Török, T., Vršnak, B.: 2017, The physical processes of CME/ICME evolution. *Space Sci. Rev.* **212**, 1159. DOI. ADS.

Martínez Oliveros, J.-C., Hudson, H.S., Hurford, G.J., Krucker, S., Lin, R.P., Lindsey, C., Couvidat, S., Schou, J., Thompson, W.T.: 2012, The height of a white-light flare and its hard X-ray sources. *Astrophys. J. Lett.* **753**, L26. DOI. ADS.

Marubashi, K., Lepping, R.P.: 2007, Long-duration magnetic clouds: a comparison of analyses using torus- and cylinder-shaped flux rope models. *Ann. Geophys.* **25**, 2453. DOI. ADS.

Marubashi, K., Cho, K.-S., Kim, Y.-H., Park, Y.-D., Park, S.-H.: 2012, Geometry of the 20 November 2003 magnetic cloud. *J. Geophys. Res.* **117**, A01101. DOI. ADS.

Marubashi, K., Akiyama, S., Yashiro, S., Gopalswamy, N., Cho, K.-S., Park, Y.-D.: 2015, Geometrical relationship between interplanetary flux ropes and their solar sources. *Solar Phys.* **290**, 1371. DOI. ADS.

Masson, S., Antiochos, S.K., DeVore, C.R.: 2013, A model for the escape of solar-flare-accelerated particles. *Astrophys. J.* **771**, 82. DOI. ADS.

Mays, M.L., Taktakishvili, A., Pulkkinen, A., MacNeice, P.J., Rastätter, L., Odstrcil, D., Jian, L.K., Richardson, I.G., LaSota, J.A., Zheng, Y., Kuznetsova, M.M.: 2015, Ensemble modeling of CMEs using the WSA-ENLIL+Cone model. *Solar Phys.* **290**, 1775. DOI. ADS.

Metcalf, T.R., Alexander, D.: 1999, Coronal trapping of energetic flare particles: Yohkoh/HXT observations. *Astrophys. J.* **522**, 1108. DOI. ADS.

Moore, R.L., Sterling, A.C., Hudson, H.S., Lemen, J.R.: 2001, Onset of the magnetic explosion in solar flares and coronal mass ejections. *Astrophys. J.* **552**, 833. DOI. ADS.

Möstl, U.V., Temmer, M., Veronig, A.M.: 2013, The Kelvin–Helmholtz instability at coronal mass ejection boundaries in the solar corona: observations and 2.5D MHD simulations. *Astrophys. J. Lett.* **766**, L12. DOI. ADS.

Murphy, N.A., Raymond, J.C., Korreck, K.E.: 2011, Plasma heating during a coronal mass ejection observed by the Solar and Heliospheric Observatory. *Astrophys. J.* **735**, 17. DOI. ADS.

Odstrcil, D.: 2003, Modeling 3-D solar wind structure. *Adv. Space Res.* **32**, 497. DOI. ADS.

Owens, M.J., Démoulin, P., Savani, N.P., Lavraud, B., Ruffenach, A.: 2012, Implications of non-cylindrical flux ropes for magnetic cloud reconstruction techniques and the interpretation of double flux rope events. *Solar Phys.* **278**, 435. DOI. ADS.

Pal, S., Nandy, D., Srivastava, N., Gopalswamy, N., Panda, S.: 2018, Dependence of coronal mass ejection properties on their solar source active region characteristics and associated flare reconnection flux. *Astrophys. J.* **865**, 4. DOI. ADS.

Plowman, J., Kankelborg, C., Martens, P.: 2013, Fast differential emission measure inversion of solar coronal data. *Astrophys. J.* **771**, 2. DOI. ADS.

Qiu, J., Yurchyshyn, V.B.: 2005, Magnetic reconnection flux and coronal mass ejection velocity. *Astrophys. J. Lett.* **634**, L121. DOI. ADS.

Qiu, J., Hu, Q., Howard, T.A., Yurchyshyn, V.B.: 2007, On the magnetic flux budget in low-corona magnetic reconnection and interplanetary coronal mass ejections. *Astrophys. J.* **659**, 758. DOI. ADS.

Richardson, I.G., Cane, H.V.: 2004, Identification of interplanetary coronal mass ejections at 1 AU using multiple solar wind plasma composition anomalies. *J. Geophys. Res.* **109**, A09104. DOI. ADS.

Richardson, I.G., Cane, H.V.: 2010, Near-Earth interplanetary coronal mass ejections during Solar Cycle 23 (1996 – 2009): catalog and summary of properties. *Solar Phys.* **264**, 189. DOI. ADS.

Rodkin, D., Goryaev, F., Pagano, P., Gibb, G., Slemzin, V., Shugay, Y., Veselovsky, I., Mackay, D.H.: 2017, Origin and ion charge state evolution of solar wind transients during 4 – 7 August 2011. *Solar Phys.* **292**, 90. DOI. ADS.

Rodkin, D., Slemzin, V., Zhukov, A.N., Goryaev, F., Shugay, Y., Veselovsky, I.: 2018, Single ICMEs and complex transient structures in the solar wind in 2010 – 2011. *Solar Phys.* **293**, 78. DOI. ADS.

Rollett, T., Möstl, C., Temmer, M., Frahm, R.A., Davies, J.A., Veronig, A.M., Vršnak, B., Amerstorfer, U.V., Farrugia, C.J., Žic, T., Zhang, T.L.: 2014, Combined multipoint remote and in situ observations of the asymmetric evolution of a fast solar coronal mass ejection. *Astrophys. J. Lett.* **790**, L6. DOI. ADS.

Sauvaud, J.-A., Larson, D., Aoustin, C., Curtis, D., Médale, J.-L., Fedorov, A., Rouzaud, J., Luhmann, J., Moreau, T., Schröder, P., Louarn, P., Dandouras, I., Penou, E.: 2008, The IMPACT Solar Wind Electron Analyzer (SWEA). *Space Sci. Rev.* **136**, 227. DOI. ADS.

Scherrer, P.H., Schou, J., Bush, R.I., Kosovichev, A.G., Bogart, R.S., Hoeksema, J.T., Liu, Y., Duvall, T.L., Zhao, J., Title, A.M., *et al.*: 2012, The Helioseismic and Magnetic Imager (HMI) investigation for the Solar Dynamics Observatory (SDO). *Solar Phys.* **275**, 207. DOI. ADS.

Share, G.H., Murphy, R.J., White, S.M., Tolbert, A.K., Dennis, B.R., Schwartz, R.A., Smart, D.F., Shea, M.A.: 2018, Characteristics of late-phase >100 MeV gamma-ray emission in solar eruptive events. *Astrophys. J.* **869**, 182. DOI. ADS.

Shen, F., Wu, S.T., Feng, X., Wu, C.-C.: 2012, Acceleration and deceleration of coronal mass ejections during propagation and interaction. *J. Geophys. Res.* **117**, A11101. DOI. ADS.

Shen, J., Zhou, T., Ji, H., Wiegelmann, T., Inhester, B., Feng, L.: 2014, Well-observed dynamics of flaring and peripheral coronal magnetic loops during an M-class limb flare. *Astrophys. J.* **791**, 83. DOI. ADS.

Slemzin, V., Chertok, I., Grechnev, V., Ignat'ev, A., Kuzin, S., Pertsov, A., Zhitnik, I., Delaboudinière, J.-P.: 2004, Multi-wavelength observations of CME-associated structures on the Sun with the CORONAS-F/SPIRIT EUV telescope. In: Stepanov, A.V., Benevolenskaya, E.E., Kosovichev, A.G. (eds.) *Multi-Wavelength Investigations of Solar Activity*, *IAU Symp.* **223**, 533. DOI. ADS.

Uralov, A.M.: 1990, The flare as a result of cross-interaction of loops – Causal relationship with a prominence. *Solar Phys.* **127**, 253. DOI. ADS.

Uralov, A.M., Lesovoi, S.V., Zandanov, V.G., Grechnev, V.V.: 2002, Dual-filament initiation of a coronal mass ejection: Observations and model. *Solar Phys.* **208**, 69. DOI. ADS.

Uralov, A.M., Grechnev, V.V., Rudenko, G.V., Myshyakov, I.I., Chertok, I.M., Filippov, B.P., Slemzin, V.A.: 2014, A challenging solar eruptive event of 18 November 2003 and the causes of the 20 November geomagnetic superstorm. III. Catastrophe of the eruptive filament at a magnetic null point and formation of an opposite-handedness CME. *Solar Phys.* **289**, 3747. DOI. ADS.

Vandas, M., Romashets, E.P.: 2003, A force-free field with constant alpha in an oblate cylinder: A generalization of the Lundquist solution. *Astron. Astrophys.* **398**, 801. DOI. ADS.

Vandas, M., Romashets, E., Geranios, A.: 2015, Modeling of magnetic cloud expansion. *Astron. Astrophys.* **583**, A78. DOI. ADS.

Vršnak, B., Žic, T., Vrbanec, D., Temmer, M., Rollett, T., Möstl, C., Veronig, A., Čalogović, J., Dumbović, M., Lulić, S., Moon, Y.-J., Shanmugaraju, A.: 2013, Propagation of interplanetary coronal mass ejections: the drag-based model. *Solar Phys.* **285**, 295. DOI. ADS.

Vršnak, B., Temmer, M., Žic, T., Taktakishvili, A., Dumbović, M., Möstl, C., Veronig, A.M., Mays, M.L., Odstrčil, D.: 2014, Heliospheric propagation of coronal mass ejections: comparison of numerical WSA-ENLIL+Cone model and analytical drag-based model. *Astrophys. J. Suppl.* **213**, 21. DOI. ADS.

Švestka, Z.: 2001, Varieties of coronal mass ejections and their relation to flares. *Space Sci. Rev.* **95**, 135. ADS.

Wood, B.E., Howard, R.A., Linton, M.G.: 2016, Imaging prominence eruptions out to 1 AU. *Astrophys. J.* **816**, 67. DOI. ADS.

Yashiro, S., Gopalswamy, N., Michalek, G., St. Cyr, O.C., Plunkett, S.P., Rich, N.B., Howard, R.A.: 2004, A catalog of white light coronal mass ejections observed by the SOHO spacecraft. *J. Geophys. Res.* **109**, A07105. DOI. ADS.

Yurchyshyn, V., Hu, Q., Abramenko, V.: 2005, Structure of magnetic fields in NOAA active regions 0486 and 0501 and in the associated interplanetary ejecta. *Space Weather* **3**, S08C02. DOI. ADS.

Zhang, J., Dere, K.P., Howard, R.A., Kundu, M.R., White, S.M.: 2001, On the temporal relationship between coronal mass ejections and flares. *Astrophys. J.* **559**, 452. DOI. ADS.

Zurbuchen, T.H., Richardson, I.G.: 2006, In-situ solar wind and magnetic field signatures of interplanetary coronal mass ejections. *Space Sci. Rev.* **123**, 31. DOI. ADS.